Seismic Reflection Imaging of Karst in the Persian Gulf; Implications for the Characterization of Carbonate Reservoirs

Caroline M. Burberry[1], Christopher A-L. Jackson[2] and Shelby R. Chandler[1]

[1]Department of Earth and Atmospheric Sciences, University of Nebraska-Lincoln, Lincoln, NE, USA

[2]Basins Research Group (BRG), Department of Earth Science and Engineering, Imperial College, London, SW7 2BP, England, UK

Acknowledgements

We thank W.D. DeMis, S.C. Ruppel and an anonymous reviewer for their detailed comments on an earlier version of this manuscript. We thank GGS ASA for the use of the PC 2000 dataset and permission to publish the results of this study. S.R.C acknowledges a UCARE grant from the University of Nebraska-Lincoln in support of her undergraduate research. We also thank IHS for permitting use of The Kingdom Suite software through an academic license to the University of Nebraska-Lincoln.

Abstract

Karstification positively and negatively impacts the quality of carbonate reservoirs; for example, dissolution and brecciation can increase porosity and permeability, whereas cavern collapse or cementation driven by post-karstification fluid flow may occlude porosity and reduce permeability. Karst may also pose challenges to drilling due to the unpredictable and highly variable porosity and permeability structure of the rock, and the corresponding difficulty in predicting drilling mud-weight. When combined, outcrop, petrographic and geochemical data can constrain the style, distribution and origin of seismic-scale karst, which may provide an improved understanding of carbonate reservoir architecture and allow development of safer drilling programs. However, relatively few studies have utilized seismic reflection data to characterize the regional development of seismic-scale karst features. In this study we use time-migrated 2D seismic reflection data to determine the distribution, scale and genesis of karst in a 3 km (9800 ft) thick, Jurassic-Miocene carbonate-dominated succession in the Persian Gulf. We map 43 seismic-scale karst features, which are expressed as vertical pipes columns of

chaotic reflections capped by downward-deflected depressions that are onlapped by overlying strata. The columns are up to 2 km (6500 ft) tall, spanning the Upper Jurassic to Upper Cretaceous succession, and are up to 5.5 km (18,000 ft) in diameter. We interpret these pipes formed in response to hypogene karstification by fluids focused along pre-existing faults, with hypogene-generated depressions enhanced by epigene processes during key intervals of exposure. Our study indicates that seismic reflection data can and should be used in conjunction with petrographic and geochemical techniques to determine the presence of hypogene karst plays, and to help improve the characterization of carbonate reservoirs and associated drilling hazards.

Introduction

Karstification can positively impact the physical and geometric properties of carbonate reservoirs (e.g. thickness, porosity, permeability, continuity, heterogeneity, and seal effectiveness). For example, dissolution during exposure and karstification can enhance porosity and permeability of otherwise tight, low-quality reservoirs. However, karstification can also have a negative impact on carbonate reservoirs by, for example, reducing reservoir thickness during periods of exposure and erosion. In addition, porosity reduction may occur as collapsed caves fill with brecciated material or fine-grained sediment (Loucks & Handford, 1992; Loucks & Mescher, 2002; Loucks, 1999), or if pore space is occluded by precipitation of hydrothermal dolomite (Davies & Smith, 2006; Smith, 2006). Furthermore, seal quality may be reduced due to the collapse and deformation of strata overlying karstified intervals (Dembicki & Machel, 1996; Cerepi et al., 2003; Vahrenkamp et al., 2004). Carbonate reservoirs affected by karstification are thus likely to be highly heterogeneous, particularly with respect to porosity and permeability, and to become more heterogeneous as the extent of karstification increases (McMechan et al., 2002; Hollis, 2011). The characterization of heterogeneity in extensive carbonate reservoirs should consider the possibility of multiple zones of enhanced porosity and permeability within the reservoir, as well as the potential for connectivity by zones of enhanced dissolution (Machel et al., 2012). Key unknowns in carbonate exploration are the extent of karstification and whether the effects on porosity and permeability are positive or negative. In the case of porosity and permeability increase, karstification poses challenges for drilling, as the porosity and permeability structure of the unit is highly unpredictable. This leads to a corresponding difficulty in predicting drilling mud-weight.

Karst features can develop either by epigene (relatively shallow) or hypogene (deep) processes. The principal difference between these two sets of processes is the origin of the dissolving fluid (Loucks, 1999). During epigene karstification, the dissolving fluid is meteoric in origin, and karstification is controlled by the shallow groundwater system developed either at the exposed surface or due to the influence of percolating meteoric water (Palmer, 1991; Loucks, 1999; Klimchouk, 2009a, b). Epigene karstification leads to the development of depressions and fissures on the exposed surface, as well as enhanced dissolution at the approximate level of the water table (Stafford et al., 2008). Extended periods of exposure can lead to the generation of caverns at or near the water table, which ultimately collapse, forming sinkholes that may extend upward to the exposed surface (Loucks, 1999; Loucks & Mescher, 2002). Depressions formed by surface dissolution are expected to show a positive linear relationship between width and depth on the paleo-exposure surface, which is not noted for collapse-related sinkholes (Stafford et al., 2008b). Caverns formed by epigene karstification are expected to be filled with breccia and cave-sediments (Loucks & Handford, 1992). Several episodes of karstification may lead to coalescence of several generations of collapsed caverns (Loucks, 1999). In contrast, during hypogene karstification, the dissolving fluid is not meteoric in origin but typically enters the system and is recharged from below (Palmer, 1991; Davies & Smith, 2006; Smith, 2006: Klimchouk, 2009a, b; Dublyansky, 2014). The migrating fluid may be associated with the expulsion of hydrocarbons (Machel et al., 2012) or the dissolution of evaporite-bearing horizons (Loucks & Handford, 1992). During hypogene karstification, dissolution of carbonate or evaporite material occurs at depth, with eventual cavern collapse forming structures similar to those formed under epigene conditions. Hypogene karstification is often associated with hydrothermal dolomite precipitation, which may partially occlude any generated porosity (Smith, 2006). The classic example for this type of karst-enhanced hydrocarbon reservoir is the Albion-Scipio Field in the Michigan Basin, Michigan, USA (Harding, 1974; Davies & Smith, 2006; Smith 2006). Geochemical analysis of pore-filling cements may be required in order to determine the source of the fluid in regions of karst features formed by collapse (Onac, 2014; Polyak et al., 2014). Hypogene features have typically been challenging to identify from seismic data, as indicated by the unexpected discovery of the Albion-Scipio Field (Harding, 1974). Epigene features, due to the smaller scale, close to sub-seismic resolution, are also challenging to identify and to predict based on seismic data (Zeng, 2011).

We here use a 2D seismic reflection dataset covering c. 8800 km^2 (3400 square miles) in the Persian Gulf, offshore central Iran to constrain the geometry, distribution and origin of karst features developed in a Jurassic-to-Cretaceous carbonate succession, and to assess how karstification impacted reservoir

architecture and heterogeneity. Seismic reflection data are a valuable tool for assessing the extent and scale of karstification, as seismic data is areally extensive compared to borehole and outcrop data. Thus, large-scale features can be mapped and heterogeneity characterized on the reservoir-scale, which may not be possible with borehole data or outcrop analogs, with the former being 1D and the latter being quasi-3D at best. We chose to study the Persian Gulf because the Mesopotamian Basin is known to have undergone at least one extended period (ca. 4 Myr) of subaerial exposure-related karstification during the Late Cretaceous (Hollis, 2011). In fact, a number of unconformities, of variable areal extent and duration, are observed in the predominantly marine, carbonate-bearing sedimentary sequence comprising the Mesopotamian Basin fill (Sharland et al., 2001; Alavi, 2004; Hajikazemi et al., 2010). Repeated exposure of Upper Cretaceous carbonates resulted in extensive karstification along the Turonian Unconformity, a regionally extensive surface developed across the Persian Gulf (Figure 1; Farzadi, 2006; Farzadi & Hesthammer, 2007; Hajikazemi et al 2010; Hollis, 2011, Hollis & Sharp 2011, Hajikazemi et al., 2012; Mehrabi & Rahimpour-Bonab, 2014). Field and core-based studies indicate that the Sarvak Formation, which immediately underlies the unconformity and which represents one of the main hydrocarbon reservoirs onshore Iran, is extensively karstified on a range of scales, containing small vugs, large caves, and up to 10 m deep depressions (Alavi, 2004; Hajikazemi et al., 2010; Hollis & Sharp, 2011; Hajikazemi et al., 2012). However, the full extent and scale of karstification in the Persian Gulf, and the effect it has on the properties of carbonate-dominated, reservoir-prone sequences, are largely unknown (Hollis & Sharp, 2011). Our key aim is thus to characterize the scale and distribution, and to infer on the origin of, large-scale karst features within the Upper Jurassic-to-Upper Cretaceous succession imaged in this part of the Persian Gulf. By comparing our purely seismic reflection-based observations with onshore outcrop analog data, we also speculate how karstification may have impacted reservoir properties in the studied succession and, potentially, in karst-impacted successions in other carbonate reservoirs.

Permian-Cretaceous Tectonostratigraphy of the Persian Gulf

The study area is located offshore from the Fars Zone, Iran, thus we use Fars region stratigraphic nomenclature (James & Wynd, 1965; Sharland et al., 2001). Furthermore, we use the sequence stratigraphic framework of Alavi (2004). Prior to the development of the Paleocene-Recent foreland basin, the study area was covered by Permian-Cretaceous carbonate platform deposits, with facies changes influenced in part by deformation related to movement on pre-existing faults (Burberry, 2015).

Many of the important pre-existing faults are Late Precambrian and have been intermittently active as oblique-slip faults since their formation (Edgell, 1996; Sharland *et al*., 2001; Cosgrove et al., 2009; Burberry et al., 2011; Burberry, 2015). One such fault is the north-trending Kazerun Fault (Figure 1), which extends offshore from the Fars region into the study area (Burberry et al., 2011).

During the Late Permian to Triassic, the study area formed part of the passive margin of the northern Arabian plate (Sharland et al., 2001). Two megasequences (Megasequences III and IV; *sensu.* Alavi, 2004) were deposited during the Permian and Triassic (Figure 2), in an equatorial, epi-Pangean shallow sea periodically affected by back-arc rifting (Sharland et al., 2001; Alavi, 2004). Each megasequence is characterized by a basal siliciclastic unit that is overlain by evaporitic, pelletal or oolitic carbonates, which alternate with dolomites (Konyuhov & Maleki, 2006). The basal units of Megasequence III comprise the Late Permian Faraghan and Dalan formations. The Dalan Formation is unconformably overlain by the Triassic Kangan Formation, with both units, which were dolomitized during shallow burial, having been deposited on the inner regions of a homoclinal carbonate ramp (Konyuhov & Maleki 2006; Esrafili-Dizaji & Rahimpour-Bonab, 2009). The Kangan Formation is overlain by the evaporite-rich Dashtak Formation, which forms part of Megasequence IV (Figure 2).

Megasequence V is Jurassic in age and was deposited when the study area was part of the Neo-Tethyan continental shelf, which was periodically shallow enough to be represented by an evaporite-bearing sabkha environment (Figure 2; Alavi, 2004). Siltstones of the Early Jurassic Neyriz Formation at the base of Megasequence V are overlain by carbonates and evaporites of the Mid-Late Jurassic Surmeh Formation. The upper part of the Surmeh Formation consists of tidal flat deposits of interlayered carbonate and evaporite (Alsharhan & Kendall, 1986; Mahari & Karimbad, 2013). The Surmeh Formation is overlain by the Tithonian Hith Anyhdrite (Beydoun et al., 1992, Sharland et al., 2001, Sepehr & Cosgrove 2005 & Fard et al., 2006), an evaporite unit deposited in a series of isolated, intra-shelf basins that developed in response to activity on pan-African faults (Alavi, 2004).

After a regional depositional hiatus in the late Tithonian (Sharland et al., 2001), carbonate deposition resumed in the Early Cretaceous with the Fahliyan Formation (Figure 2). The Fahliyan Formation grades upwards into the shale-dominated Gadvan Formation, which in turn is overlain by the Aptian Dariyan Formation, another carbonate-dominated succession (Alavi 1994). The end of the Aptian was marked by the development of another key regional unconformity (Sharland et al., 2001), which may have been related to a slight fall in eustatic sea level (Figure 2). Deposition of megasequence VIII (Albian-Turonian) began with the deposition of the mixed carbonate-siliciclastic Kazhdumi Formation, which is overlain by

the Cenomanian-Turonian Sarvak Formation (James & Wynd 1965, Koop & Stoneley 1982, Alavi 2004, Sepehr & Cosgrove 2007; Van Buchem et al., 2011). The Sarvak Formation was deposited during a global highstand (Figure 2) that triggered a basin-wide, transgressive, carbonate-dominated sequence to be deposited across much of the Persian Gulf (Farzadi, 2006; Hajikazemi et al., 2010). Facies within the Sarvak Formation can be separated into distinct carbonate platforms and intrashelf basinal carbonates, potentially related to reactivation on pre-existing faults and salt movement (Esrafili-Dizaji & Rahimpour-Bonab, 2009; Van Buchem et al., 2011; Mehrabi & Rahimpour-Bonab 2014).

The Turonian Unconformity formed during a short sea-level lowstand (Figure 2) driven by regional uplift and halokinesis, and by ophiolite obduction onto both the Omani and Iranian margins (Bashari, 2007; Ali & Watts, 2009; Hajikazemi et al 2010; Soleimany & Sabat 2010; Ali et al., 2013). Subaerial exposure of the Sarvak Formation at the Turonian Unconformity lasted for ca. 4 Myr and led to the generation of a major paleokarst (Farzadi, 2006; Farzadi & Hesthammer 2007; Hollis, 2011; Hollis & Sharp, 2011; Hajikazemi et al., 2012; Rahimpour-Bonab et al., 2012; Mehrabi & Rahimpour-Bonab 2014). Karstification at the Turonian Unconformity was enhanced by a warm and humid climate, which was associated with heavy rainfall (Hajikazemi et al., 2010; Mehrabi & Rahimpour-Bonab, 2014). The Turonian Unconformity is overlain by the deposition of the first foreland megasequence related to the development of the Zagros Orogen (Gurpi, Ilam and Laffan formations; Figure 2) in the Coniacian-Maastrichtian. The Gurpi Formation consists of argillaceous lime mudstones, whereas the Laffan and Ilam formation comprise carbonate and shale sequences (James & Wynd 1965, Koop & Stoneley 1982, Alavi 2004, Sepehr & Cosgrove 2007). A further regional unconformity, driven by local tectonics and a eustatic sea level lowstand, defines the top of the Maastrichtian (Figure 2; Sharland et al., 2001).

Methods

We use a grid of 2D seismic reflection data (line length c. 7000 km/4300 miles, areal extent c. 8800 km^2/3400 square miles line spacing c. 2 km/6500 ft) offshore from the Fars Zone to map seismic-scale karst features developed along key unconformities (Figure 3). These data are in two-way time (TWT) and no depth conversion has been undertaken. However, given that the units of interest are mostly above major evaporite horizons, lateral velocity variations in the overburden are minimal and assumed not to significantly impact our structural interpretation. Exploration wells IMD-1 and IE-1 (D-1 and E-1 of Swift et al. 1998) lie in the NW corner of the survey region, with data from these wells being used to pick a total of nine seismic horizons (Figure 4). The TWT to each seismic horizon was calculated from data

given in Swift et al. (1998) and the appropriate age was assigned to each horizon; top Messininan, top Chattian, top Maastrichtian, top Turonian, top Aptian, top Tithonian, top Callovian, top Norian and top Changhsingian. Within the Permian-Cretaceous sequence, the top Maastrichtian, top Turonian, top Aptian, top Norian and top Changhsingian (see above and Figure 2; Alavi, 2004), which correspond to unconformities mapped or described within the Persian Gulf by other workers (e.g. Alsharhan & Nairn, 1995, Swift et al., 1998). The top Callovian reflection lies within the Surmeh Formation, is tied to wells D-1 and E-1 (Swift et al., 1998), and underlies the largely transparent seismic facies of the Upper Jurassic package (Figure 4). The top Tithonian reflection marks the end of the Late Jurassic depositional hiatus and is distinguished by a clear reflection event overlying a transparent seismic facies (Figure 4). The Coniacian-Maastrichtian foreland basin sequence is marked by NE-dipping clinoforms in the NE part of the dataset (Burberry et al., 2011). Our top Chattian reflection is equivalent to the "top Asmari" marker of Swift et al. (1998).

After it was mapped, we created and contoured a two-way time structure map for each horizon. In the displayed maps, contours were typically spaced at 0.015 s TWT (c. 62 m/203 ft for Cretaceous horizons and c. 77 m/252 ft for Jurassic horizons and the top Norian horizon) and no smoothing was applied. We inspected each contour map and individual seismic line for deflections in each horizon, paying particular attention to areas where there were chaotic reflections beneath the deflected regions. We recorded the location of each deflection in both map view and on the nearest intersecting seismic lines. We also measured the width and depth of the deflection on each key reflection, on both NW- and NE-oriented seismic lines. Given the resolution of the seismic data, measurements of width and depth were made to the nearest 100 meters. Lastly, we made a series of isochron (time-thickness) maps of key units between the mapped horizons. These maps and measurements allow the dimensions and distribution of the deflections to be described and correlated between horizons, and the processes involved in their formation to be inferred.

Basin structure

Baaske et al. (2007) and Burberry et al. (2011) provide a detailed discussion of the basin structure in the area of study. We here provide a very brief review of the basin structure, as several structural features are important in the context of the genesis of the karst-related structures forming the focus of this paper. A time-structure map of the top Norian illustrates a series of NW-SE-striking normal faults and

two prominent domes (Figure 5a). The NW-trending dome in the SW corner of the dataset is the south-eastern tip of the Golshan structure and the dome in the southernmost corner of the dataset is the northern tip of the anticline forming the South Pars Field (Bordenave, 2003). In addition to these domes, a series of fault sets are visible on this surface, the A, B, E and K structures (Bordenave, 2003) and the X and Z fault sets (Figure 5a). Lastly, there is a N-trending high located close to the offshore trend of the Kazerun Fault; Burberry et al. (2011) interpret this as a salt wall related to halokinesis triggered by Cretaceous movement of the Kazerun Fault (see also Fard et al., 2006). The faults mapped at top Norian level are not observed on and thus die-out below the Turonian Unconformity. Rather, this surface dips gently to the NE, and a series of low-amplitude anticlines are identified in the NE of the dataset (Figure 5b; Burberry et al., 2011). Subtle indicators of the Golshan and South Pars structures are still visible on the Turonian Unconformity, as is the N-trending high located near the offshore trace of the Kazerun Fault (Figure 5b).

Seismic expression of deflection features

Forty-three large depressions are identified in this dataset, discernible both on structure maps and in seismic cross-sections. Each of these features can be identified on the top Callovian, top Tithonian, top Aptian and top Turonian reflections. The contoured top-structure maps indicate the depressions are sub-circular, with two notable sub-circular depressions being indicated by the black boxes on Figure 6, corresponding to seismic lines and features discussed later in the text. The two boxed features are clearly sub-circular on the top Turonian reflection, but their morphology varies slightly with depth (Figure 6). The sub-circular features are only weakly expressed on the top Tithonian and top Callovian surfaces (Figure 6a, 6b) and the overall structure of these surfaces is similar to that of the top Norian (Figure 5a). In contrast, the features are clearly visible on the overlying top Turonian and top Aptian surfaces (Figures 6c, 6d) as depressions on these overall NE-dipping surfaces. This suggests that the magnitude of the deflections dies out downwards. Sub-circular depressions identified in map view are characterized by marked downward deflections in horizons identified on both NW- and NE-trending cross-sections. Figure 7 shows the two crossing seismic lines for the northernmost boxed feature on Figure 6. Deflections on successively younger horizons directly overlie depressions on underlying horizons, forming near-vertical columns, subsequently referred to as “pipes”, of disturbed reflections. Away from the pipes, the stratigraphy is expressed by continuous parallel reflectors (Figure 7a-d). The top Norian and top Changhsingian reflections are undeformed. A detailed view of the pipe shown in

Figure 7 is shown in Figure 8. Thickening can be observed within the top Aptian-top Turonian package (marked as X on Figure 8) and thinning is noted in the upper part of the top Callovian-top Norian package (marked as Y on Figure 8). Thinning can also be observed in the top Tithonian-top Callovian package, which will be discussed later.

On the top Callovian surface, the features are 0.3-6.1 km wide, on average 2.6 km wide (980-20,000 ft wide, average 8500 ft) and c. 51-307 m deep, on average 144 m deep (70-1,000 ft, average 470 ft) Deflections on this surface show no clear relationship (positive or negative) between width and depth (Figure 9a). On the top Tithonian surface, the features are 0.7-5.9 km wide, on average 2.6 km wide (2,300-19,300 ft, average 8,500 ft) and c. 26-359 m deep, on average 146 m deep (85-1,200 ft, average 480 ft), thus are essentially the same size as those on the underlying top Callovian surface, although there is a very weak positive linear relationship between width and depth (Figure 9b). On the top Aptian surface the features are generally wider than on the lower two surfaces described above (1.4-7.1 km wide, with an average of 2.9 km/4,600-23,000 ft wide, average 9,500 ft) but are shallower (c. 40-247 m deep, with an average depth of 117 m/131-810 ft, average 384 ft). Again, there is a weak (R^2=0.29) positive relationship between feature width and depth (Figure 9c). On the top Turonian surface, the features are 0.9-5.6 km wide, average 2.8 km deep (2,900-18,300 ft, average 9200 ft) and c. 20-247 m deep/66-810 ft deep (average 89 m/290 ft), thus are smaller than those developed on the underlying top Aptian surface. There is a weak positive linear relationship between deflection width and depth with an R^2 value of 0.32 (Figure 9d).

About 25% of the pipes are expressed on the top Maastrichtian reflection, where they are 1.2-9.5 km wide and 40-247 m deep (3,900-31,100 ft wide, 131-810 ft deep). Deflections are typically onlapped by overlying Paleocene clastic units, which thicken into the depressions (Figure 10). Figure 10 shows the crossing lines that define the southern boxed area on Figure 6, and highlights the large, pipe-like nature of the feature. There is a very weak (R^2=0.17) linear relationship between the width and depth the deflection on the top Maastrichtian reflection (Figure 11a). Top Maastrichtian deflections are typically located above the largest deflection features noted on other reflections (Figure 6), that is, features deeper than 0.02 s TWT and wider than 2 km/6,500 ft (Figure 11b). We note that the top Chattian reflection, which overlies the top Maastrichtian reflection, is rarely deflected downward above any of the features (Figure 10).

Beneath each of the 43 features identified in our dataset, we observe thinning of the seismic package between the top Tithonian and top Callovian reflections (Figure 12, see also Figures 7 and 10). This

package contains the Jurassic Hith Anhydrite and the upper part of the Jurassic Surmeh Formation (Figure 2). Altogether, this package thins from c. 510 m/1600 ft in the overall dataset (450-500 m/1400-1640 ft thick in wells D-1 and E-1 near the study area according to Swift et al., 1998; wells marked on Figure 3) to c. 250 m/820 ft beneath many of the deflection features, representing thinning of c. 50%. The seismic package between the top Callovian and top Norian reflections, the remainder of the Jurassic Surmeh Formation, also thins beneath the deflections (Figure 13, see also Figures 7, 8 and 10). This Lower and Middle Jurassic package thins from c. 900 m/2,900 ft thick in the overall dataset (350-400 m/1,150-1,300 ft thick in wells D-1 and E-1 near the study area according to Swift et al., 1998; wells marked on Figure 3) to c. 450 m/1,400 ft thick beneath the pipes, again representing thinning of c. 50%.

The 43 features described above are not evenly distributed across the study area, but are most common in the southern part of the dataset, close to the South Pars Field (Figure 14, see also Figure 5). Within the cluster of features around South Pars Field, there are two subtle linear trends (arrowed on Figure 14). These linear trends appear to be associated spatially with faults A and B (Figure 15, see also Figure 5). Faults A and B displace the Triassic and older horizons by c. 90 m/300 ft, and are overlain by large depressions in the Aptian and Turonian reflections. In addition, a few features are spatially associated with Fault K (arrowed on Figure 14). Figure 16 illustrates a subtle depression on the Aptian reflection above Fault K that has affected not only the Triassic and older horizons (as in the case of Faults A and B), but also the Jurassic and some Early Cretaceous units as well. Some of the faults in the dataset are associated with significant zones of chaotic reflection events beneath the top Changhsingian reflection (e.g. Figure 15b) even though the offset on the top Changhsingian reflection may be quite small (c. 70 m). Some of the faults in the dataset are associated with deflections in the top Maastrichtian reflection, but there is no apparent systematic relationship between faulting and top Maastrichtian deflection.

In summary, 43 pipe-like zones of distorted and downward deflected reflection events are observed in the dataset, extending from the top Callovian up to the top Turonian reflection event; occasionally these zones and the associated downward deflection extend over a vertical distance of 1500-2100 m/4,900-6,900 ft and are expressed at the top Maastrichtian reflection. On the top Turonian and top Aptian reflections there is a weak (R^2= 0.32 and 0.29 respectively linear relationship between deflection width and depth, although the features are, on average, wider and deeper on the top Aptian reflection than on the top Turonian reflection, thus they narrow and become shallower upwards. The width-depth relationship is less pronounced on the top Jurassic reflection and is not present for the features at the

top Callovian reflection. Marked thinning occurs in the evaporite-bearing Jurassic section beneath the pipe-like features (Figure 8).

Interpretation

Based on the carbonate-dominated nature of the studied succession and the observed map and cross-sectional geometry of the pipes, we interpret them as features formed by karstification. The vertical extent of the features, and their spatial relationship to seismically imaged faults, suggest they formed by dominantly hypogene processes. In this model, an aggressive fluid capable of dissolving large amounts of calcium carbonate preferentially flowed up the fault zones, dissolving the host rock, and causing overlying stratigraphy to collapse downwards and generate the sag features observed along key unconformities (Figure 17a). The seismic lines show thickness changes in the top Tithonian-top Callovian and top Callovian-top Norian packages (Figure 8), corresponding to the Jurassic Hith Anhydrite-Upper Surmeh Formation and the Surmeh and Neyriz Formations, respectively. The rugose nature of the top Tithonian reflection suggests more dissolution has occurred in the top Tithonian-top Callovian package than in the top Callovian-top Norian package, and that large-scale dissolution occurred in the Hith Anhydrite and parts of the Surmeh Formation. The thickness variation in the top Callovian-top Norian package illustrated in Figure 8 suggests that dissolution in this package preferentially occurred in specific horizons, such as evaporite layers within the Surmeh Formation. The dissolution of evaporites by formation water expelled from lower, siliciclastic units such as the Faraghan Formation, is expected to produce an aggressive fluid suitable for creating the overlying karst pipes (Chapman, 1987; Bjørlykke, 1993; Bjorkum & Nadeau, 1998). By analogy with other hypogene karst zones, such as those developed in the Albion-Scipio field, Michigan, USA (Harding, 1974; Davies & Smith, 2006), the column of disturbed reflections associated with each feature, as observed in the seismic lines, is likely to represent a zone of brecciation, potentially partly cemented by minerals precipitated as fluid flow continued along the faults post-collapse.

However, the weak, positive linear relationship between width and depth observed at the top Turonian and top Aptian reflections is not expected with hypogene karstification processes (Stafford et al., 2008b). Rather, this linear relationship suggests that existing depressions above hypogene pipes were enhanced by epigene processes during subaerial exposure during the Late Aptian and Late Turonian (Figure 17b, c). We suggest that existing depressions and brecciated zones would allow increased

meteoric water percolation into the host rock at the depressions, thus driving deepening and widening of the already formed surface depression.

Thus, we propose a two-phase model for the formation of the observed karst features (Figure 17). We infer that during Phase 1, hypogene karstification and initial development of karst pipes occurred immediately prior to the sub-aerial exposure of the region during the Aptian. Formation water expelled from the underlying Faraghan Formation caused dissolution of the evaporite layers in the Surmeh Formation and the Hith Anhydrite, creating the aggressive fluid necessary to cause large-scale dissolution as the fluid moved up fault zones (Figure 17a). In addition, the mixing of aggressive hypogene fluids and meteoric water during exposure enhanced the width and depth of depressions observed on this seismic horizon (Figure 17b). The sedimentary layers overlying the pre-Aptian pipes would have subsided, creating depressions on Aptian-Turonian horizons and possible thickening of sedimentary fill into those depressions.

During Phase 2, we infer that karstification also occurred during the period of prolonged (c. 4 Myr) occurring in Turonian exposure and recorded by the Turonian unconformity (Figure 17c) (Hollis, 2011). This period of sub-aerial exposure resulted in dissolution of exposed carbonates, resulting in widening and deepening of sinkholes formed over the hypogene pipes. A subsequent rise in relative sea level led to deposition of the Coniacian-Maastrichtian succession, which underwent differential compaction over the rugose Turonian unconformity (Figure 17d), and which resulted in sinkholes in the much shallower, top Maastrichtian reflection above the largest of the Turonian and earlier sinkholes. Onlap of Palaeogene strata onto the top Maastrichtian sinkholes indicate that these features formed at this time (Figure 17d).

Discussion

The model in Figure 17 proposes that the karst features observed in the Persian Gulf, offshore the Fars Region formed by dominantly hypogene processes, overprinted by epigene processes. Most hypogene karst are quite linear due to their spatial and ultimately genetic relationship with fractures or faults (Hurley & Budros, 1990; Palmer, 1991; Davies & Smith, 2006; Smith, 2006; Klimchouck, 2009). The examples cited in our study appear to form as a series of columns broadly aligned with regional fault trends, although they cannot confidently be mapped as long, linear trends, given the spacing (c. 2 km/6,500 ft) of the seismic lines. We further interpret that existing sag structures are enhanced by

365 epigene processes during known periods of exposure associated with the formation of the regional end-
366 Aptian and end-Turonian unconformities. A short period of exposure immediately followed deposition
367 of the Hith Anhydrite, thus dissolution of the Hith Anhydrite, and initial cavern development, may have
368 begun earlier than our model proposes (Alavi, 2004). It is therefore possible that caverns formed by
369 epigene processes may have existed before the main phase of hypogene fluid flow. Several other short
370 periods of exposure are documented during the Cenomanain to Turonian, suggesting that there were
371 likely several phases of enhancement of the initial karst features and that there may be numerous levels
372 of sub-seismic scale, epigene karst in the Cretaceous carbonate sequence (Hajikazemi et al., 2012;
373 Mehrabi & Rahimpour-Bonab 2014).

374 We speculate that sub-seismic scale caverns and collapse features formed by epigene processes occur
375 on the Aptian and Turonian exposure surfaces, within the upper 100 m of the exposed carbonates.
376 Similar features are noted in high-resolution seismic lines in the Tarim Basin (Zeng et al., 2011). Areally
377 extensive, but moderate-scale epigene karstification is observed on the Turonian unconformity (e.g. c. 2
378 m high caves : Hajikazemi et al., 2010) in the Dezful Embayment, Iran (van Buchem et al., 2011;
379 Rahimpour-Bonab et al., 2012) and offshore Iran (Taghavi et al., 2006), in addition to oil-fields offshore
380 UAE (Videtich et al., 1988) and offshore Qatar (Hollis, 2011). All of these locations, including the
381 location of the present study area, fall within the area predicted to have been subaerially exposured
382 during plate flexure-driven subsidence (Patton & O'Connor, 1998; Hollis, 2011; Casini et al., 2011),
383 suggesting that tectonics and eustacy were crucial factors driving end-Turonian karstification. In
384 addition to long-wavelength tectonics, Cretaceous halokinesis, associated with the reactivation of pan-
385 African age faults, has been inferred based on seismic data in the Persian Gulf (Baaske et al. 2007;
386 Soleimany & Sabat, 2010; Burberry et al., 2011). The South Pars structure in the southeast of our dataset
387 falls on a N-trending pan-African fault, and is thought to be salt-cored at depth (Edgell, 1996; Bordenave,
388 2003). Enhanced uplift around this salt dome may have led to the exposure of the South Pars area
389 earlier than the remainder of the study area. This enhanced uplift may explain why more seismic-scale
390 sinkholes are mapped in the southeast corner of the dataset (Figure 13).

391 Large-scale sinkholes formed by a series of processes similar to the model proposed here are
392 documented in carbonate reservoirs worldwide. One such example occurs in the Upper Devonian
393 Grosmont reservoir, Alberta, Canada. Here, the Woodbend Group, an interbedded carbonate, marl and
394 evaporite unit, underwent salt dissolution, fracture generation and several periods of epigene
395 karstification, as well as a prolonged period of hypogene karstification (Machel et al., 2012). Karst

features are represented by 30-150 m diameter, circular-to-oval depressions, formed by a combination of dissolution at depth, subsequent collapse, and enhancement of the surface depressions by epigene dissolution (Dembicki & Machel, 1996; Machel et al., 2012).

Additional examples of hypogene karst and speleogenesis come from the Pecos River Valley in New Mexico and West Texas (Stafford et al., 2008a, b). Evidence for hypogene karstification includes the presence of abundant breccia pipes, collapse structures and the presence of cross-formational brecciation (Stafford et al., 2008b). In this region, caverns such as Coffee Cave contain numerous large, vertical risers connecting levels of the cave system developed along fracture pathways (Stafford et al., 2008b). However, in contrast to those in our study area, vertical risers in Coffee Cave are only a few meters tall. Within the same region, the Yates Field, developed in the San Andres dolomite, is characterized as a karstified structure. Typical of hypogene karst zones, the most intense karstification occurs along the highly fractured region on the crest of the anticline (Stafford et al., 2008a, b). Core data confirm the presence of collapse breccias and cave cements in this field (Craig, 1998). Karst features in the Yates Field are again smaller than our examples (Stafford et al., 2008a). However, hypogene karst features occur at a range of scales, as noted from the c. 200 m high Albion-Scipio field mentioned in previous sections (Harding 1974).

Karstification and reservoir properties

Hypogene karst pipes such as the ones described in this study are likely to be comprised of collapse breccia, which are defined as a mass of angular, chaotic displaced clasts (Loucks and Handford, 1992). This collapse breccia forms as fluids moving up fault zones and dissolve lower material, causing subsidence in the overlying rock mass. The halo around the pipe is expected to be a crackle breccia zone, defined by Loucks & Handford (1992) as intensely fractured rock, but with little to no displacement of the clasts. This zone is anticipated to be formed as fluid percolates away from the master fault into associated fracture systems. Thus, porosity and permeability in these zones are increased, with a porosity up to 15% in some collapse breccia zones and up to 5% in the crackle breccia zones (Loucks & Mescher, 2002). Corresponding permeability values may be up to several darcys for the collapse breccia and tens to hundreds of millidarcys for the crackle breccia zones (Loucks and Mescher, 2002).

Karstification can have both a positive and a negative effect on the porosity and permeability of a reservoir. Karst features and associated breccias may initially act as a conduit for fluid flow, and in the

case of cave networks, may enhance reservoir connectivity. However, further cave collapse may also act to reduce porosity and permeability. Subsequent fluid migration may also precipitate minerals that partially or fully occlude any earlier generated porosity. Equally, extensive karstification may breach or compromise the seal unit, as overlying clastic units collapse into sinkholes under differential compaction. For example, in the Boonsville gas field, Texas collapse chimneys in the Ellenburger Formation create reservoir compartments in the overlying clastic sequence (Hardage et al., 1996). Within the carbonate itself, karstification first generated and then destroyed large-scale porosity and permeability as the chimneys collapsed (Lucia, 1995).

Our study demonstrates that hypogene karst features overprinted by epigene processes can be identified from seismic data. The Upper Surmeh unit (part of the package showing localized thinning between the top Callovian and top Tithonian reflections; Fig. 11) is age-equivalent to the Arab Formation, an important reservoir unit around the Persian Gulf. We suggest that the Arab Formation may also be affected by these hypogene karst structures, particularly in regions where paleohighs developed as a result of faulting and halokinesis (Hajikazemi et al., 2010; Mehrabi & Rahimpour-Bonab, 2014). The hypogene karst play is one that should be considered in future exploration in the Persian Gulf region and in other carbonate-dominated zones worldwide. In order to effectively assess the potential for karstification and the positive or negative impacts on a field-scale, workflows should integrate regional tectonostratigraphic analysis, regional to field-scale seismic analysis, and assessment of diagenetic processes through geochemical analysis and petrography.

Conclusions

This study has documented the presence of seismic-scale karst pipe features in a dataset from the Persian Gulf. The features form vertical pipes which are between 1500-2100 m/4,900-6,900 ft in height, spanning the Upper Jurassic to Turonian (in some cases, Maastrichtian) sedimentary units. The associated depressions range in diameter from 0.9-5.6 km/2,900-18,300 ft on the Turonian unconformity. The features cluster near known faults in the dataset, and this, coupled with the vertical pipe morphology, leads us to suggest a dominantly hypogene formation process. Fluids expelled from the underlying Faraghan Formation dissolve the Upper Jurassic Hith Anhydrite and existing evaporite lenses within the Jurassic Surmeh Formation, creating an aggressive fluid that is then transported up fault zones, creating the vertical pipes. The weak linear relationship between width and depth on both

456 the Aptian and Turonian unconformities suggests that epigene processes enhanced the existing
457 depressions during times of exposure. During continued deposition, the Coniacian to Maastrichtian
458 strata underwent differential compaction over the uneven Turonian surface, creating depressions over
459 the largest of the Turonian sinkholes. Depressions in the Maastrichtian surface marker unit were then
460 infilled by the Paleocene strata.

461 The vertical pipes are likely to be filled with collapse breccia, and to be surrounded by a halo of crackle
462 breccia, locally enhancing the porosity and permeability in the reservoir units. The hypogene karst play
463 is one that should be considered in future exploration in the Persian Gulf region and in other carbonate-
464 dominated zones worldwide. In order to effectively assess the potential for karstification and the
465 positive or negative impacts on a field-scale, workflows should integrate regional tectonostratigraphic
466 analysis, regional to field-scale seismic analysis, and assessment of diagenetic processes through
467 geochemical analysis and petrography.

468

469 **References**

470 Alavi, M. 1994. Tectonics of the Zagros orogenic belt of Iran: new data and interpretations.
471 Tectonophysics v. 229, p. 211-238.

472 Alavi, M., 2004. Regional stratigraphy of the Zagros fold-thrust belt of Iran and its proforeland
473 evolution. American Journal of Science, v. 304 p. 1-20

474 Ali, M.Y. & Watts, A. B., 2009. Subsidence history gravity anomalies and flexure of the United Arab
475 Emirates (UAE) foreland basin. Geoarabia, v. 14 (2) p. 17-44

476 Ali, M.Y., Watts, A. B. & Searle, M. P., 2013. Seismic stratigraphy and subsidence history of the United
477 Arab Emirates (UAE) rifted margin and overlying foreland basins. In Al Hosani, K. et al., (eds) Lithosphere
478 dynamics and sedimentary basins: The Arabian Plate and Analogues. Frontiers in Earth Sciences, p. 127-
479 143

480 Alsharhan, A.S. & Kendall, C. G. St C. 1986. Precambrian to Jurassic rocks of Arabian Gulf and Adjacent
481 areas: Their facies, Depositional setting and hydrocarbon habitat. AAPG Bulletin, v. 70 (8) p. 977-1002.

482 Alsharhan, A. S. & Nairn, A. E. M. 1995. Tertiary of the Arabian Gulf - Sedimentology and Hydrocarbon
483 Potential. Palaeogeography Palaeoclimatology Palaeoecology v. 114, p. 369-384.

484 Baaske, U. P., Mutti, M., Baioni, F., Bertozzi, G. & Naini, M. A., 2007. Using multi-attribute neural
485 networks classification for seismic carbonate facies mapping: a workflow example from the mid-
486 Cretaceous Persian Gulf deposits. In Davies, R. J., Posamentier, H. W., Wood, L. J. & Cartwright, J. A.
487 (eds), Seismic Geomorphology. Geological Society of London Special Publication v. 277 p. 105-120

488 Bashari, A., 2007. Integrated 3D seismic and petrophysical data of the Sarvak Formation in the Persian
489 Gulf. First Break, v. 25, p. 45-53

490 Beydoun, Z .R, Hughes Clarke, M. W. & Stonely, R. 1992. Petroleum in the Zagros Basin: A late Tertiary
491 Foreland Basin Overprinted onto the outer edge of a vast hydrocarbon-rich Paleozoic-Mesozoic passive-
492 margin shelf. In: MacQueen, R. & Leckie, D. (eds) Foreland Basins and Foldbelts. Memoirs, American
493 Association of Petroleum Geologists, v. 55, p. 309–339

494 Bjorkum, P. A. & Nadeau, P., 1998. Temperature controlled porosity/permeability reduction, fluid
495 migration and petroleum exploration in sedimentary basins. APPEA Journal, v. 38, p. 453-464

496 Bjorlykke, K., 1993. Fluid flow in sedimentary basins. Sedimentary Geology v. 86, p. 137-158

497 Bordenave, M.L., 2003. Gas prospective areas in the Zagros domain of Iran and in the Gulf Iranian
498 waters. AAPG Search and Discovery article 10040a.

499 Burberry, C. M., Jackson, C. A-L. & Cosgrove, J. W., 2011. Late Cretaceous to Recent deformation related
500 to inherited structures and subsequent compression within the Persian Gulf: a 2D seismic case study.
501 Journal of the Geological Society of London, v. 168, p. 485-498.

502 Burberry, C. M., 2015. The effect of basement fault reactivation on the Triassic-Recent geology of
503 Kurdistan, N Iraq. Journal of Petroleum Geology, v. 38 (1) p. 37-58.

504 Casini, G., Gillespie, P. A., Verges, J., Romaire, I., Fernandez, N., Casciello, E., Saura, E., Mehl, C., Homke,
505 S., Embry, J-C., Aghajari, L. & Hunt, D.W., 2011. Sub-seismic fractures in foreland fold and thrust belts:
506 insight from the Lurestan Province, Zagros Mountains, Iran. Petroleum Geoscience, v. 17, p. 263-282

507 Cerepi, A., Barde, J-P. & Labat, N., 2003. High-resolution characterization and integrated study of a
508 reservoir formation: the Danian carbonate platform in the Aquitaine Basin (France). Marine and
509 Petroleum Geology v. 20, p. 1161-1183

510 Chapman, R.E., 1987. Fluid flow in sedimentary basins: a geologist's perspective. In Goff, J.C. & Williams,
511 B.P.J. (eds) Fluid Flow in Sedimentary Basins and Aquifers. Geological Society Special Publication 34 p3-
512 18

513 Cosgrove, J. W., Talbot, C. J. & Aftabi, P., 2009. A train of kink folds in the surficial salt of Qum Kuh,
514 Central Iran. Journal of Structural Geology, v. 31, p. 1212-1222.

515 Craig, D. H., 1998. Caves and other features of Permian karst in San Andres dolomite, Yates field
516 reservoir, west Texas." In James, N.P. & Choquette, P.W. (eds) *Paleokarst* p. 342-363.

517 Davies, G. R. & Smith, L. B. Jr., 2006. Structurally controlled hydrothermal dolomite reservoir facies: An
518 overview. AAPG Bulletin v. 90, p. 1641-1690

519 Dembicki, E. A. & Machel, H. G., 1996. Recognition and delineation of Paleokarst zones by the use of
520 wireline logs in the bitumen-saturated upper Devonian Grosmont Formation of Northeastern Alberta,
521 Canada. AAPG Bulletin v. 80 (5) p. 695-712

522 Dublyansky, Y. V., 2014. In Klimchouk, A., Sasowsky, I., Mylroie, J. & Engel, S. A. (eds). Hypogene cave
523 morphologies. Selected papers and abstracts of the symposium held February 2-7 2014, San Salvador
524 Island, Bahamas. Karst Waters Institute Special Publication v.18, p. 1-3

525 Edgell, H. S. 1996. Salt Tectonism in the Persian Gulf Basin. In: Salt Tectonics (edited by Alsop, G. I.,
526 Blundell, D. J. & Davison, I.). Geological Society of London Special Publication v. 100, p. 129-151.

527 Esrafili-Dizaji, B. & Rahimpour-Bonab, H., 2009. Effects of depositional and diagenetic characteristics on
528 carbonate reservoir quality: a case study from the South Pars gas field in the Persian Gulf. Petroleum
529 Geoscience v. 15 p. 325—344

530 Fard, I.A., Braathen, A., Mokhtari, M. & Alavi, S. A. 2006. Interaction of the Zagros Fold-Thrust Belt and
531 the Arabian-type, deep-seated folds in the Abadan Plains and the Dezful Embayment, SW Iran.
532 Petroleum Geoscience v. 12, p. 347-362

533 Farzadi, P., 2006. The development of Middle Cretaceous carbonate platforms, Persian Gulf, Iran:
534 constraints from seismic stratigraphy, well and biostratigraphy. Petroleum Geoscience v. 12, p. 59-68

535 Farzadi, P. & Hesthammer, J., 2007. Diagnosis of the upper Cretaceous paleokarst and turbidite systems
536 from the Iranian Persian Gulf using volume-based multiple seismic attribute analysis and pattern
537 recognition. Petroleum Geoscience v. 13, p. 227-240

538 Hajikazemi, E., Al-Aasm, I.S. & Coniglio, M., 2010. Subaerial exposure and meteoric diagenesis of the
539 Cenomanian-Turonian Upper Sarvak Formation, southwestern Iran. In Leturmy, P. & Robin, C (eds).
540 Tectonic and stratigraphic evolution of Zagros and Makran during the Mesozoic-Cenozoic. Geological
541 Society of London Special Publication v. 330, p. 253-272.

542 Hajikazemi, E., Al-Aasm, I.S. & Coniglio, M., 2012. Chemostratigraphy of Cenomanian-Turonian
543 carbonates of the Sarvak Formation, Southern Iran. Journal of Petroleum Geology, v. 35 (2) p. 187-206

544 Hardage, B. A., Carr, D. L., Lancaster, D. E., Simmons Jr. J. L., Elphick, R. Y., Pendleton, V. M. & Johns, R.
545 A., 1996. 3-D seismic evidence of the effects of carbonate karst collapse on overlying clastic stratigraphy
546 and reservoir compartmentalization. Geophysics v. 61 (5) p. 1336-1350

547 Harding, T. P., 1974. Petroleum traps associated with wrench faults. AAPG Bulletin v. 58, p 1290-1304

548 Hollis, C. & Sharp, I., 2011. Albian-Cenomanian-Turonian carbonate-siliciclastic systems of the Arabian
549 Plate: advances in diagenesis, structure and reservoir modelling: introduction. Petroleum Geoscience, v.
550 17, p. 207-209

551 Hollis, C., 2011. Diagenetic controls on reservoir properties of carbonate successions within the Albian-
552 Turonian of the Arabian Plate. Petroleum Geoscience v. 17, p. 223-241

553 Hurley, N. F. & Budros, R., 1990. Albion-Scipio and Stoney Point fields - U.S.A. In Foster, N. H. &
554 Beaumont, E. A. (eds). Treatise Atlas: Stratigraphic Traps I, AAPG Treatise Atlas A203, p. 1-37

555 James, G. A. & Wynd, J. G. 1965. Stratigraphic nomenclature of Iranian Oil Consortium Agreement Area.
556 AAPG Bulletin v. 49(12), p. 2182-2245.

557 Jassim, S. Z. & Goff, J. C., eds. (2006): Geology of Iraq, Dolin, Prague and Moravian Museum, Bruno
558 (Czech Republic), 341pp.

559 Klimchouk, A.B., 2009a. Morphogenesis of hypogenic caves. Geomorphology v. 106, p. 100-117

560 Klimchouk, A. B., 2009b. Principal features of hypogene speleogenesis. Hypogene speleogenesis and
561 karst hydrogeology of artesian basins, v. 2009, p. 7-15

562 Konyukov, A. I. & Maleki, B., 2006. The Persian Gulf Basin: Geological History, Sedimentary Formations,
563 and Petroleum Potential. Lithology and Mineral Resources, v.41 p. 344-361

564 Koop, W. J. & Stoneley, R. 1982. Subsidence History of the Middle-East Zagros Basin, Permian to Recent.
565 Philosophical Transactions of the Royal Society of London Series a-Mathematical Physical and
566 Engineering Sciences v. 305, p. 149-168

567 Loucks, R. G., 1999. Paleocave carbonate reservoirs: Origins, Burial-depth modifications, Spatial
568 complexity, and reservoir implications. AAPG Bulletin v. 83, p. 1795-1834

569 Loucks, R. G. & Handford, C. R., 1992. Origin and recognition of fractures, breccias, and sediment fills in
570 paleocave reservoir networks. In Canderlaria, M. P. & Redd, C. L. (eds) Paleokarst, karst-related
571 diagenesis and reservoir development: Examples from Ordovician-Devonian age strat of West Texas and
572 the mid-continent. Permian Basin Section, SEPM Publication 92-33 p. 31-44.

573 Loucks, R. G. & Mescher, P. K., 2002. Paleocave facies classification and associated pore types.
574 Paleocaves Reservoirs: Origin, Spatial Complexity, and Reservoir Implications, p. 1-18

575 Lucia, F. J., 1995. Lower Paleozoic Cavern Development, Collapse, and Dolomitization, Franklin
576 Mountains, El Paso, Texas. In Budd, D. A., Saller, A. H. & Harris, P. M. (eds) Unconformities and Porosity
577 in Carbonate strata. AAPG Memoir v. 63 p. 279-300

578 Machel, H. G., Borrero, M. L., Dembicki, E., Huebscher, H., Ping, L. & Zhao, Yi., 2012. The Grosmont: the
579 world's largest unconventional oil reservoir hosted in carbonate rocks. In Garland, J., Nielson, J. E.,
580 Laubach, D. E. & Whidden, K., (eds). Advances in Carbonate Exploration and Reservoir Analysis.
581 Geological Society of London Special Publication v. 370 p. 49-81.

582 Mahari, R. & Karimbad, B. M., 2013. The microfacies and sedimentary environments of Surmeh
583 Formation in the Kish Gas Field, Persian Gulf, Iran. Journal of Basic and Applied Scientific Research v. 3
584 (3) p. 999-1004

585 McMechan, G. A., Loucks, R. G., Mescher, P. & Zeng, X., 2002. Characterization of a coalesced, collapsed
586 paleocave reservoir analog using GPR and well-core data. Geophysics v. 67 (4) p. 1148-1158

587 Mehrabi, H. & Rahimpour-Bonab, H., 2014. Paleoclimate and tectonic controls on the depositional and
588 diagenetic history of the Cenomanian-early Turonian carbonate reservoirs, Dezful Embayment, SW Iran.
589 Facies, 60, p147-167

590 Onac, B. P., 2014. Hypogene vs. Epigene caves: the sulfur and oxygen isotope fingerprint. In Klimchouk,
591 A., Sasowsky, I., Mylroie, J. & Engel, S. A. (eds). Hypogene cave morphologies. Selected papers and

592 abstracts of the symposium held February 2-7 2014, San Salvador Island, Bahamas. Karst Waters
593 Institute Special Publication 18, p. 75

594 Palmer, A. N., 1991. Origin and morphology of limestone caves. GSA Bulletin, v. 103, p. 1-21

595 Patton, T. L. & O'Connor, S. J., 1988. Cretaceous Flexural History of Northern Oman Mountain foredeep,
596 United Arab Emirates. AAPG Bulletin, v. 72 (7) p. 797-809

597 Polyak, V. J., Asmeron, Y., Hill, C. A., Palmer, A. N., Provencio, P. P., Palmer, M. V., McIntosh, W. C.,
598 Decker, D. D. & Onac, B. P., 2014. Isotopic studies of byproducts of hypogene speleogenesis and their
599 contribution to the geologic evolution of the western United States. In Klimchouk, A., Sasowsky, I.,
600 Mylroie, J. & Engel, S. A. (eds). Hypogene cave morphologies. Selected papers and abstracts of the
601 symposium held February 2-7 2014, San Salvador Island, Bahamas. Karst Waters Institute Special
602 Publication v. 18, p. 88-94

603 Rahimpour-Bonab, H., Mehrabi, H., Enayati-Bidgoli, A.H. & Omidvar, M., 2012. Coupled imprints of a
604 tropical climate and recurring emergence on reservoir evolution of a mid-Cretaceous carbonate ramp,
605 Zagros Basin, southwest Iran. Cretaceous Research, v. 37 p. 15-34.

606 Sepehr, M. & Cosgrove, J. W. 2005. Role of the Kazerun Fault Zone in the formation and deformation of
607 the Zagros Fold-Thrust Belt, Iran. Tectonics v. 24(5), Doi: 10.1029/2004TC001725

608 Sepehr, M. & Cosgrove, J. W. 2007. The role of major fault zones in controlling the geometry and spatial
609 organisation of structures in the Zagros Fold-Thrust Belt. In: Geological Society of London Special
610 Publication v. 272, p. 419-436.

611 Sharland, P. R., Archer, R., Casey, D. M., Davies, R. B., Hall, S. H., Heward, A. P., Horbury, A. D. &
612 Simmons, M. D. 2001. Arabian Plate Sequence Stratigraphy. Oriental Press, Manama, Bahrain. 371pp

613 Smith, L. B. Jr., 2006. Origin and reservoir characteristics of Upper Ordovician Trenton-Black River
614 hydrothermal dolomite reservoirs in New York. AAPG Bulletin, v. 90, p. 1691-1718

615 Stafford, R. W., Behnken, F. H. & White, J. G., 2008a. Hypogene speleogenesis within the Central Basin
616 Platform: Karst porosity in the Yates Field, Pecos County, Texas, USA. *In* Sasowsky, I. D., Feazel, C. T.,
617 Mylroie, J. E., Palmer, A. N. & Palmer M. V. (eds). Karst from Recent to Reservoirs. Karst Waters
618 Institute Special Publication v. 14, p. 174-178

Stafford, K. W., Nance, R., Rosales-Lagard, R. & Boston, P. J., 2008b. Epigene and hypogene gypsum karst manifestations of the Castile Formation: Eddy County, New Mexico and Culbertson County, Texas, USA. International Journal of Speleology v. 37 (2) p. 83-98

Swift, S. A., Uchupi, E. & Ross, D. A. 1998. Late Cenozoic Geology of the central Persian (Arabian) Gulf from Industry Well data and Seismic profiles. WHOI Technical Memorandum 01-98, 76pp.

Taghavi, A.A., Mork, A. & Emadi, M.A., 2006. Sequence stratigraphically controlled diagenesis governs reservoir quality in the carbonate Dehluran Field, southwest Iran. Petroleum Geoscience, v. 12, p. 115-126

Vahrenkamp, V. C., David, F., Duijndam, P., Newall, M. & Crevello, P., 2004. Growth architecture, faulting and karstification of a Middle Miocene carbonate platform, Luconia Province, Offshore Sarawak, Malaysia. In Seismic imaging of carbonate reservoirs and systems, AAPG Memoir v. 81, p. 329-350

Van Buchem., F. S. P., Simmons, M. D., Droste, H. J. & Davies, R. B., 2011. Late Aptian to Turonian stratigraphy of the eastern Arabian Plate – depositional sequences and lithostratigraphic nomenclature. Petroleum Geoscience v. 17, p. 211-222

Videtich, P. E, McLimans, R. A., Kim, H., Watson, H. & Nagy, R. M., 1988. Depositional, diagenetic, thermal and maturation histories of Cretaceous Mishrif Formation, Fateh Field, Dubai. AAPG Bulletin, v. 72 (10) p. 1143-1159

Zampetti, V., Marquez, X., Mukund, S., Bach, S. & Emang, M., 2014. 3D Seismic characterization of UER Karst, Offshore Qatar. IPTC paper 17638.

Zeng, H., Wang, Q., Janson, X., Loucks, R., Xia, Y., Xu, L. & Yuan, B., 2011. Characterizing seismic bright spots in deeply buried Ordovician Paleokarst strata, Central Tabei uplift, Tarim Basin, Western China. Geophysics, v. 76 p. 127-137

Author Vitae

C.M. Burberry

Caroline (Cara) Burberry received her PhD in 2008 from Imperial College, London, after which she spent time involved in petroleum exploration, with a focus on fieldwork in Kurdistan. Since 2010, she has been an Assistant Professor at the University of Nebraska-Lincoln. Her primary interests are structural

geology and petroleum exploration, using fieldwork, seismic interpretation, remote sensing, petrography and analog modeling.

C. A-L. Jackson

Christopher Jackson is currently the Statoil Professor of Basin Analysis in the Department of Earth Science and Engineering, Imperial College, United Kingdom. He obtained a B.Sc. and Ph.D. from the University of Manchester. His research interests are in the tectonostratigraphic evolution of rifts and the application of 3-D seismic data to understanding the formation and filling of sedimentary basins.

S.R.Chandler

Shelby Chandler received her B.S. Degree in Geology in 2014 from the University of Nebraska - Lincoln, where she spent her final two years of undergraduate education participating in the UCARE (Undergraduate Creative Activities and Research Experience) program. This paper details her second research project. Shelby currently lives in Concord, CA and work as a Technical Recruiter in San Francisco.

Figure Captions

Figure 1: Location map, showing the position of the study area within the wider Persian Gulf. The bounding faults of the present Zagros Orogen are marked (ZFF; Zagros Frontal Fault and HZF; High Zagros Fault) as well as a key basement fault in the region (KF: the Kazerun Fault). Black stars mark other karsted locations noted in the text. The basemap is a DEM derived from GeoMappApp.

Figure 2: Tectonostratigraphic column showing the units of interest in the Permian – Cretaceous section, together with important regional tectonic events and a global sea level curve. The global sea level curve and megasequence information are from Alavi (2004). Wavy lines denote unconformities. Arrows mark the reflection events mapped in the study. Stage names are from Sharland et al., (2001) and Alavi (2004).

Figure 3: Map showing the layout of the seismic grid in this dataset, as well as the location of the wells used for correlation and horizon identification. The black bounding polygon shows the area of the grids in Figures 5 and 14. The black rectangle shows the location of the grids in Figures 6, 12 and 13. Locations of seismic lines used in other figures are also shown.

Figure 4: Well-tie from wells given in Swift et al. (1998) to the closest seismic line and the depths in TWT of each mapped reflection on this line. Mapped reflections are arrowed on Figure 2 and the location of the seismic segment is shown on Figure 3.

Figure 5: a) top structure map of the top Norian reflection and b) top structure map of the top Turonian reflections. Fault cuts (solid black lines) and the trend of the Kazerun Fault (dashed lines) are shown. Faults and structural highs (the Golshan and South Pars structures) on the top Norian reflection are labeled after Bordenave (2003).

Figure 6: Detailed contour maps of a) the top Callovian reflection, b) the top Tithonian reflection, c) the top Aptian reflection, and d) the top Turonian reflection. Only the region where the most features are found is shown, so that detail may be seen. Sub-circular depressions can be observed in the contours. The locations of the features shown in Figures 7 and 10 are marked by white boxes. The upper white box marks the feature in Figure 7, the lower white box marks the feature in Figure 10.

Figure 7: NW (a, b) and NE-oriented (c, d) crossing lines showing the morphology of a pipe-like feature forming a vertical zone of distorted reflections. a) and c) show the uninterpreted lines, and b) and d) show the interpreted lines. Dashed lines show the interpreted pipe margins. The arrow marks the point where the lines cross. Both uninterpreted and interpreted lines are shown. The feature deforms

horizons from the top Turonian to the top Callovian reflections and significant thinning is noted in the top Tithonian-top Callovian package. The location of these seismic segments is marked on Figure 3. Tur, Turonian; Apt, Aptian; Tith, Tithonian; Callov, Callovian; Nor, Norian; Chang, Changsingian.

Figure 8: a) Reproduction of part of Figure 7d, the interpreted NE-oriented line, and b) detailed view of the reflections internal to the pipe-like feature. Two key seismic packages are marked by dashed lines. Note thickening of seismic package X (~Turonian age) into the center of the depression, indicating active subsidence during deposition of the Sarvak Formation. Seismic package Y is considerably thinned underneath the pipe-like feature, indicating removal of a near-complete layer of the Surmeh Formation. Tur, Turonian; Apt, Aptian; Tith, Tithonian; Callov, Callovian; Nor, Norian; Chang, Changsingian.

Figure 9: Graphs showing the variation in depth of the features with changing width, on the top Callovian, top Tithonian, top Aptian and top Turonian reflections. Weak positive correlation between width and depth is noted on the top Tithonian, top Aptian and top Turonian reflections, but not the top Callovian reflection. R^2 values for the best-fit line shown are noted on the graphs.

Figure 10: NW (a, b) and NE-oriented (c, d) crossing lines showing the morphology of a karst feature forming a vertical zone of distorted reflections. The arrow marks the point where the lines cross. Both uninterpreted (a, c) and interpreted (b, d) lines are shown. Vertical dashed lines mark the interpreted margins of the pipe. The feature deforms horizons from the top Maastrichtian to the top Callovian reflections and significant thinning is noted in the top Jurassic-top Callovian package. The Paleocene-Oligocene package onlaps the deflected top Maastrichtian reflection. The location of these seismic segments is marked on Figure 3. Tur, Turonian; Apt, Aptian; Tith, Tithonian; Callov, Callovian; Nor, Norian; Chang, Changsingian.

Figure 11: a) Graph showing the variation in depth of the features with changing width, on the top Maastrichtian reflection. Weak correlation between width and depth is noted. The R^2 value for the best-fit line shown are noted on the graph. b) Graph showing width-depth relationship between features on the top Turonian and top Maastrichtian reflections. Blue dots indicate features on the top Turonian reflection with no Maastrichtian counterpart; red dots indicate those Turonian features with associated Maastrichtian deflections. Larger features have associated Maastrichtian depressions.

Figure 12: Map showing the thickness variation in the top Tithonian-top Callovian seismic package, for the detailed area shown in Figure 6. Overlain black stars in part (b) indicate the locations of mapped pipe-like features, correlating to zones of thinning in this package. The locations of the features shown

in Figures 7 and 10 are marked by black boxes. The upper black box marks the feature in Figure 7, the lower black box marks the feature in Figure 10.

Figure 13: Map showing the thickness variation in the top Callovian-top Norian seismic package, for the detailed area shown in Figure 6. Overlain black stars in part (b) indicate the locations of mapped pipe-like features, correlating to zones of thinning in this package. The locations of the features shown in Figures 7 and 10 are marked by black boxes. The upper black box marks the feature in Figure 7, the lower black box marks the feature in Figure 10.

Figure 14: Top structure map of the Top Norian reflection, with associated fault cuts marked in pale grey. Structures discussed in the text are arrowed and labeled. Black stars mark the locations of mapped pipe-like features.

Figure 15: Seismic lines showing the relationship of some pipe-like features to fault structures A (a, b) and B (c, d). Refer back to Figure 5a for fault morphology. Both uninterpreted (a, c) and interpreted (b, d) lines are shown. Solid black lines mark fault planes. The vertical dashed lines mark the margins of the pipe. Note that the images shown in part (b) are of the same feature as Figure 10, but this figure is extended to depth to illustrate the fault geometry and associated reflection character. Tur, Turonian; Apt, Aptian; Tith, Tithonian; Callov, Callovian; Nor, Norian; Chang, Changsingian.

Figure 16: Seismic lines, both uninterpreted (a) and interpreted (b), showing the relationship of a pipe-like feature to fault structure K (refer back to Figure 5a for fault morphology). Solid black lines mark fault planes. Vertical dashed lines mark the edges of the pipe. Note that in this example the influence of the faulting is more prominent than the influence of dissolution. Tur, Turonian; Apt, Aptian; Tith, Tithonian; Callov, Callovian; Nor; Chang, Changsingian.

Figure 17: Conceptual diagram showing the development of the seismic-scale karst features in the study area. Formation names are labeled on the diagrams. Solid arrows represent movement of hypogene fluids, dashed lines represent movement of epigene fluids. Hatched areas represent regions of significant dissolution – the pipe-like features. a) in pre-Aptian time, fluids expelled from the Faraghan Formation migrate up faults and dissolve the Hith Formation. b) aggressive fluids from the dissolution of the evaporite percolate through the overlying layers causing dissolution, and developing depressions on the surface in the Aptian. These depressions are enhanced by percolation of meteoric water and mixing of fluids. c) as burial continues, and the surface is exposed again in the Turonian, a second phase of fluid mixing occurs and depressions on the Turonian surface related to the vertical pipes are enhanced. d) by

the Eocene, subsidence of the Gurpi Formation and overlying Paleogene sediments over the uneven Turonian surface form depressions on the top Gurpi (top Maastrichtian) which are infilled with Paleogene sediments.

Figures

Figure 1

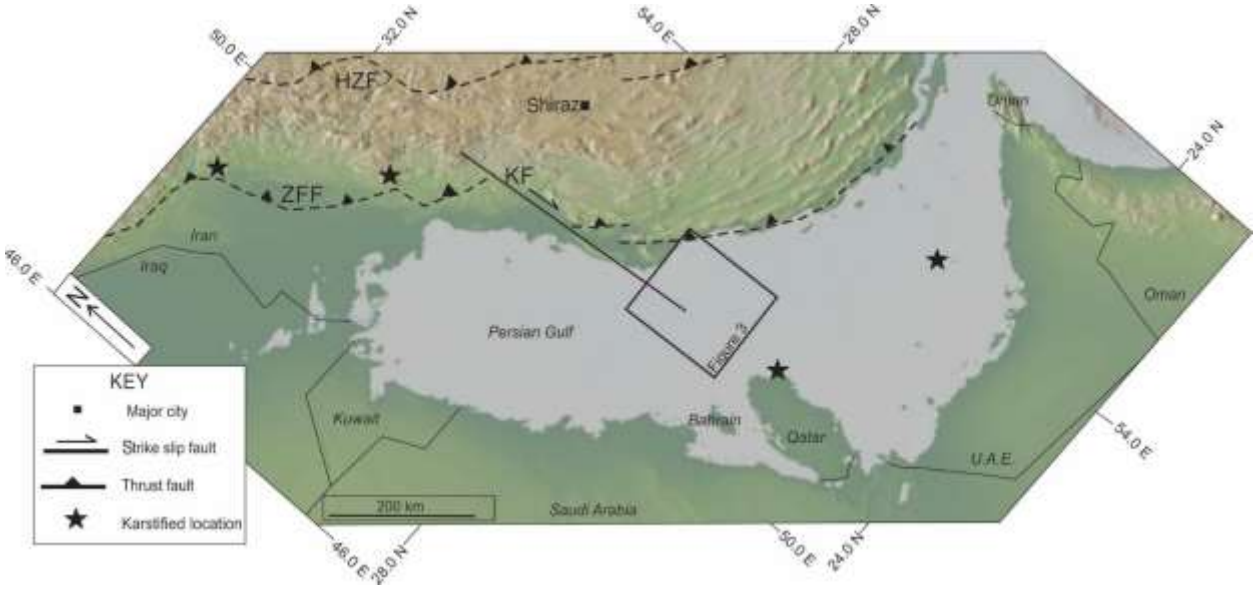

Figure 2

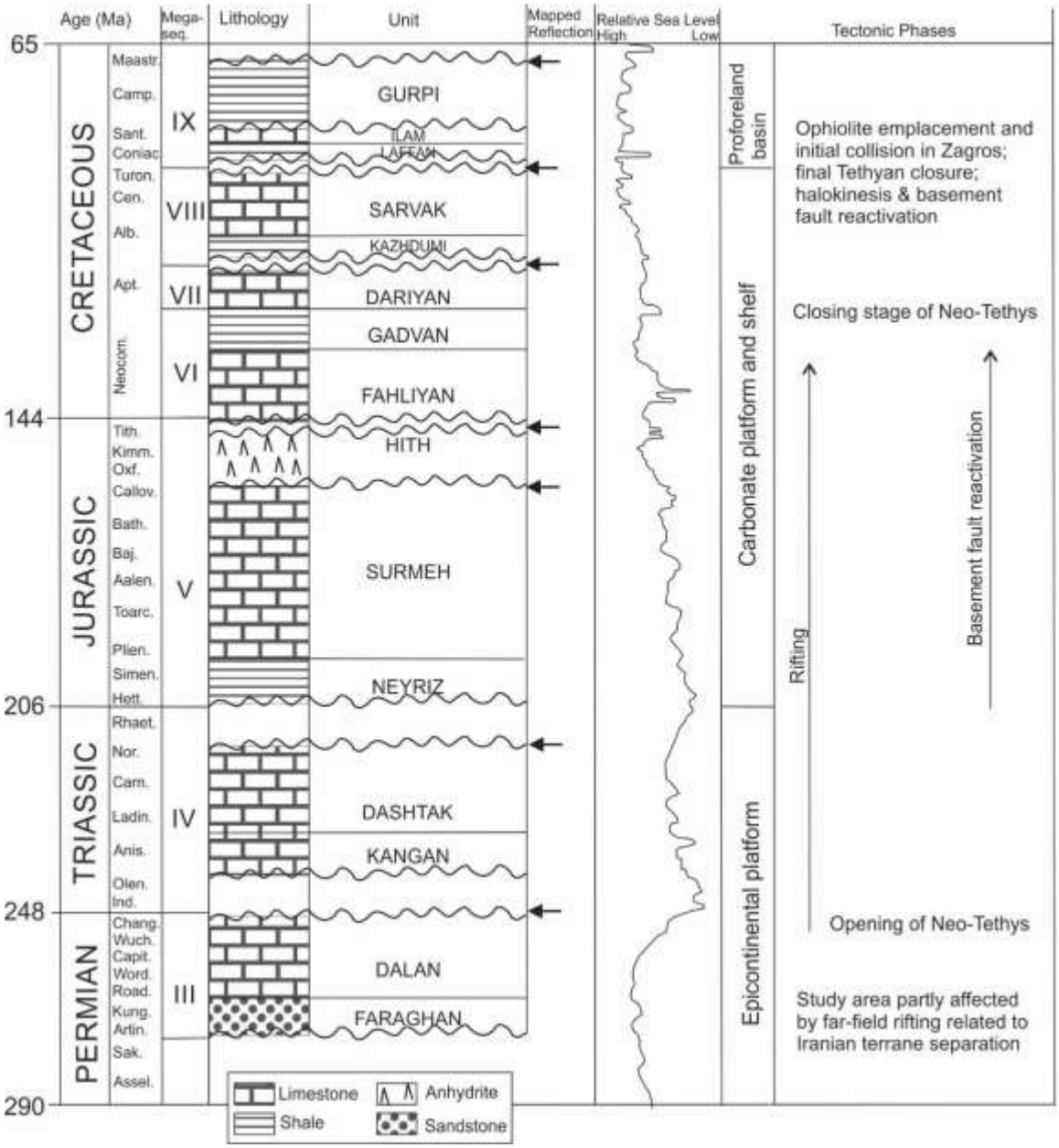
Age (Ma)
Mega-seq.
Lithology
Unit
Mapped Reflection
Relative Sea Level
High
Low
Tectonic Phases
65
144
206
248
290
CRETACEOUS
JURASSIC
TRIASSIC
PERMIAN
Maastr.
Camp.
Sant.
Coniac.
Turon.
Cen.
Alb.
Apt.
Neocom.
Tith.
Kimm.
Oxf.
Callov.
Bath.
Baj.
Aalen.
Toarc.
Plien.
Simen.
Hett.
Rhaet.
Nor.
Carn.
Ladin.
Anis.
Olen.
Ind.
Chang.
Wuch.
Capit.
Word.
Road.
Kung.
Artin.
Sak.
Assel.
IX
VIII
VII
VI
V
IV
III
GURPI
ILAM
LAFFAN
SARVAK
KAZHDUMI
DARIYAN
GADVAN
FAHLIYAN
HITH
SURMEH
NEYRIZ
DASHTAK
KANGAN
DALAN
FARAGHAN
Limestone
Anhydrite
Shale
Sandstone
Proforeland basin
Carbonate platform and shelf
Epicontinental platform
Ophiolite emplacement and initial collision in Zagros; final Tethyan closure; halokinesis & basement fault reactivation
Closing stage of Neo-Tethys
Basement fault reactivation
Rifting
Opening of Neo-Tethys
Study area partly affected by far-field rifting related to Iranian terrane separation

Figure 3

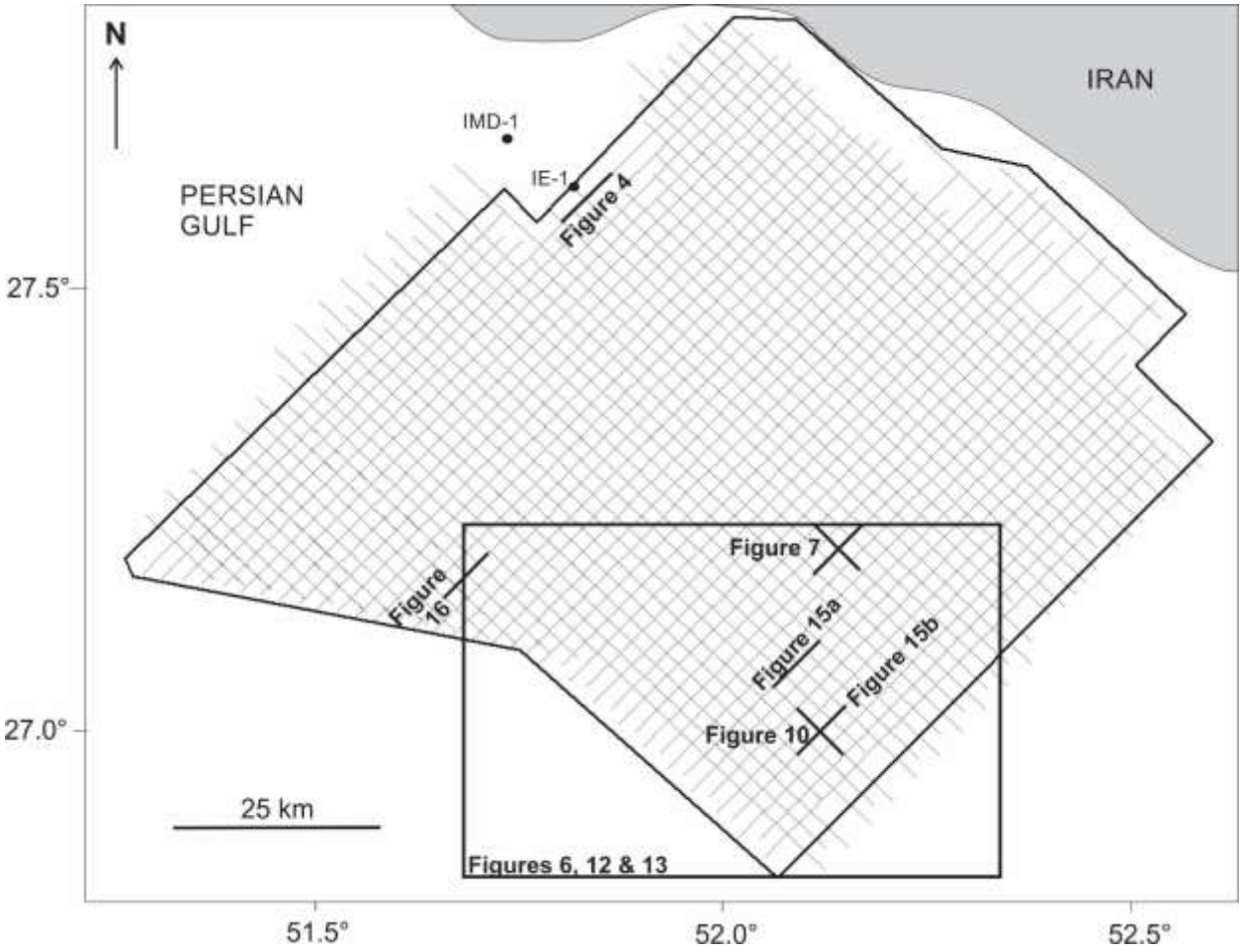
N
IRAN
IMD-1
IE-1
PERSIAN
GULF
Figure 4
27.5°
Figure 7
Figure 16
Figure 15a
Figure 15b
Figure 10
27.0°
25 km
Figures 6, 12 & 13
51.5°
52.0°
52.5°

Figure 4

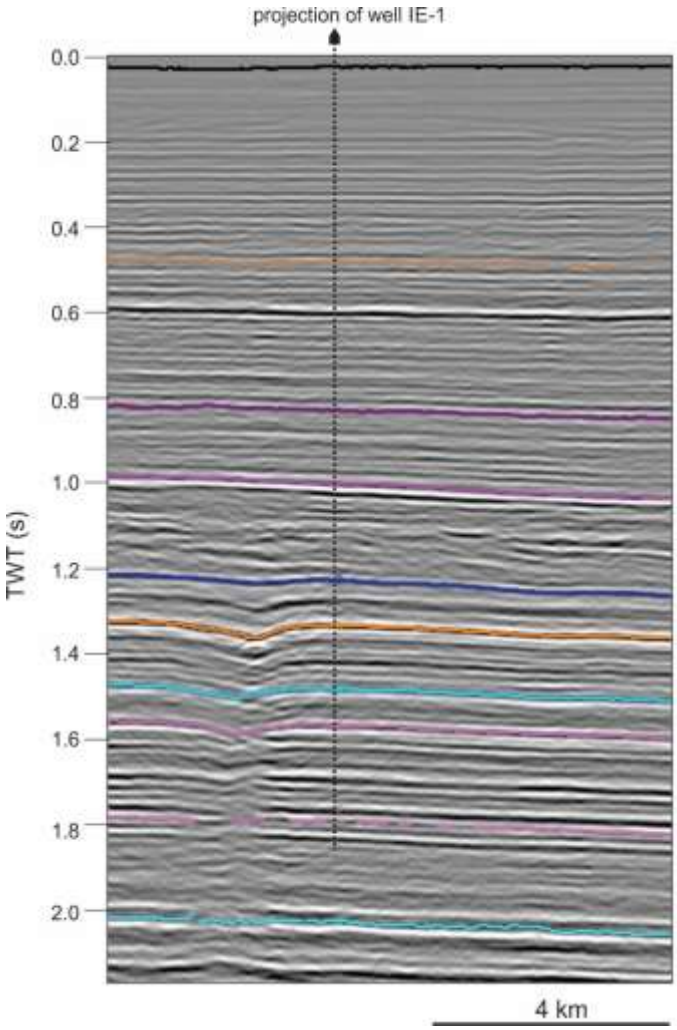

	Formation Tops in TWT (s)		Projected marker depths from this dataset in TWT (s)
	IMD-1	IE-1	
Sea floor			
Top Messinian	0.43	-	0.47
~Top Chattian (Top Asmari)	0.72	0.83	0.82
Top Maastrichtian	1.09	1.06	0.99
Top Turonian	1.2	1.11	1.21
Top Aptian	1.31	1.34	1.31
Top Tithonian	1.47	1.52	1.46
Top Callovian	1.69	1.6	1.58
Top Norian	1.84	1.67	1.76
Top Changhsingian	1.9	-	2.2

Figure 5

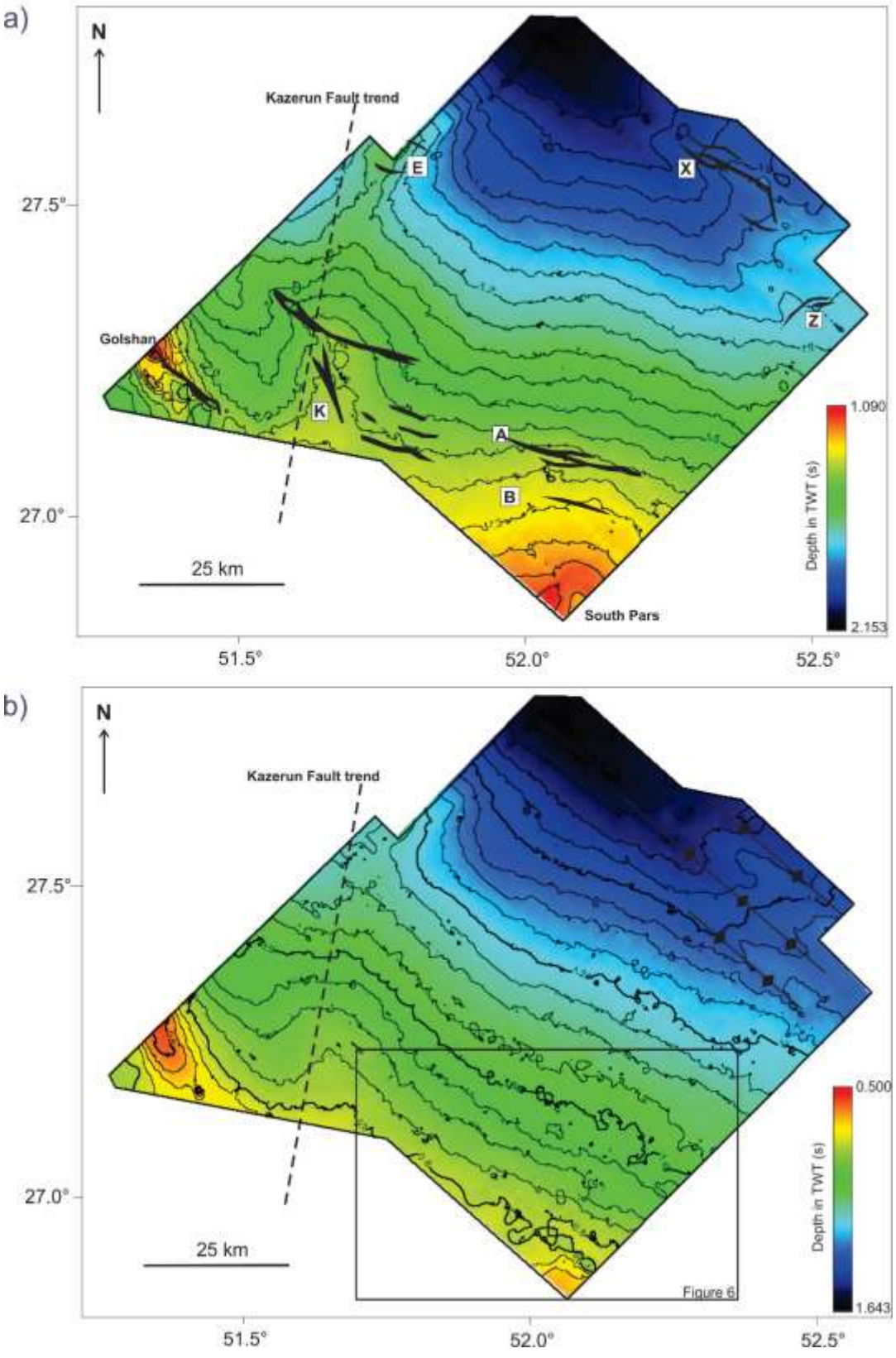
a)
N
Kazerun Fault trend
E
X
Z
Golshan
K
A
B
27.5°
27.0°
25 km
South Pars
1.090
Depth in TWT (s)
2.153
51.5°
52.0°
52.5°
b)
N
Kazerun Fault trend
27.5°
27.0°
25 km
Figure 6
0.500
Depth in TWT (s)
1.643
51.5°
52.0°
52.5°

Figure 6

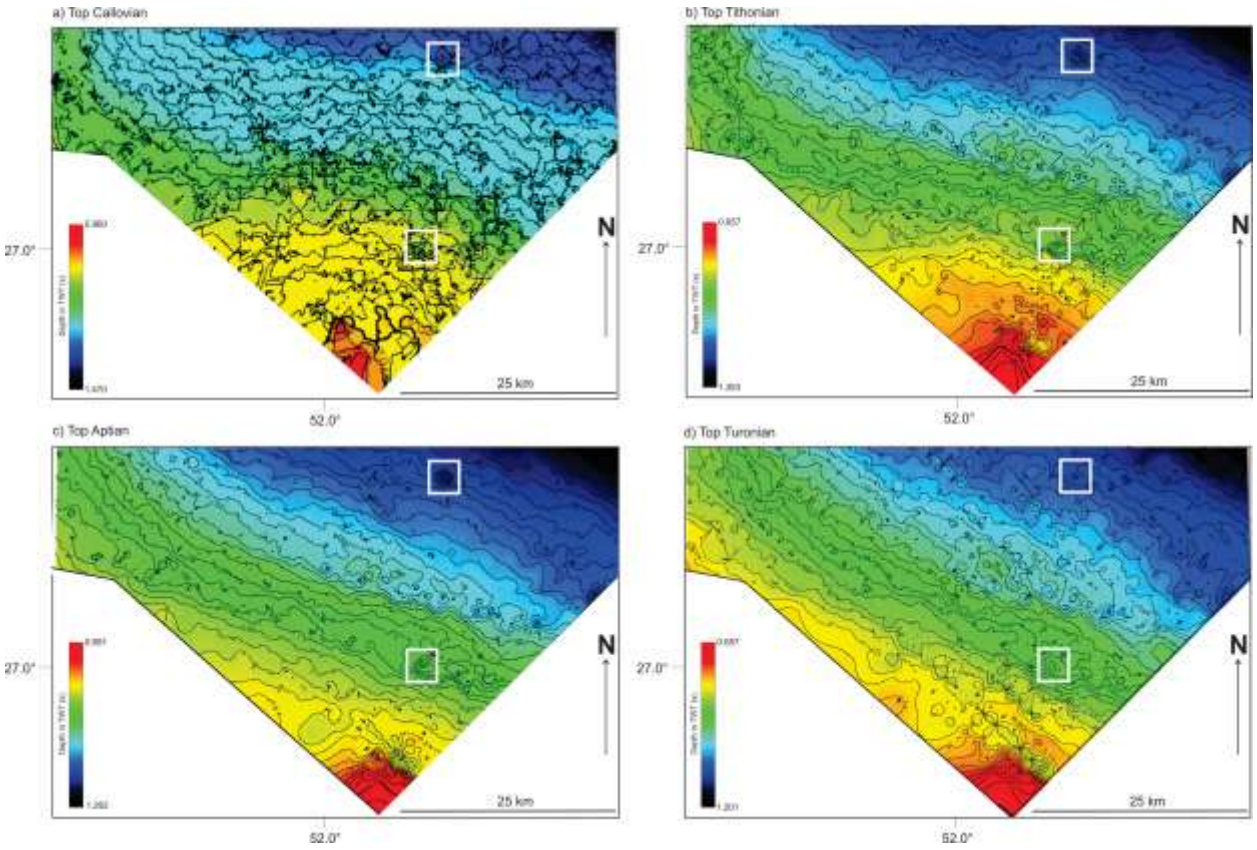
a) Top Callovian
b) Top Tithonian
c) Top Aptian
d) Top Turonian
27.0°
52.0°
N
25 km

Figure 7

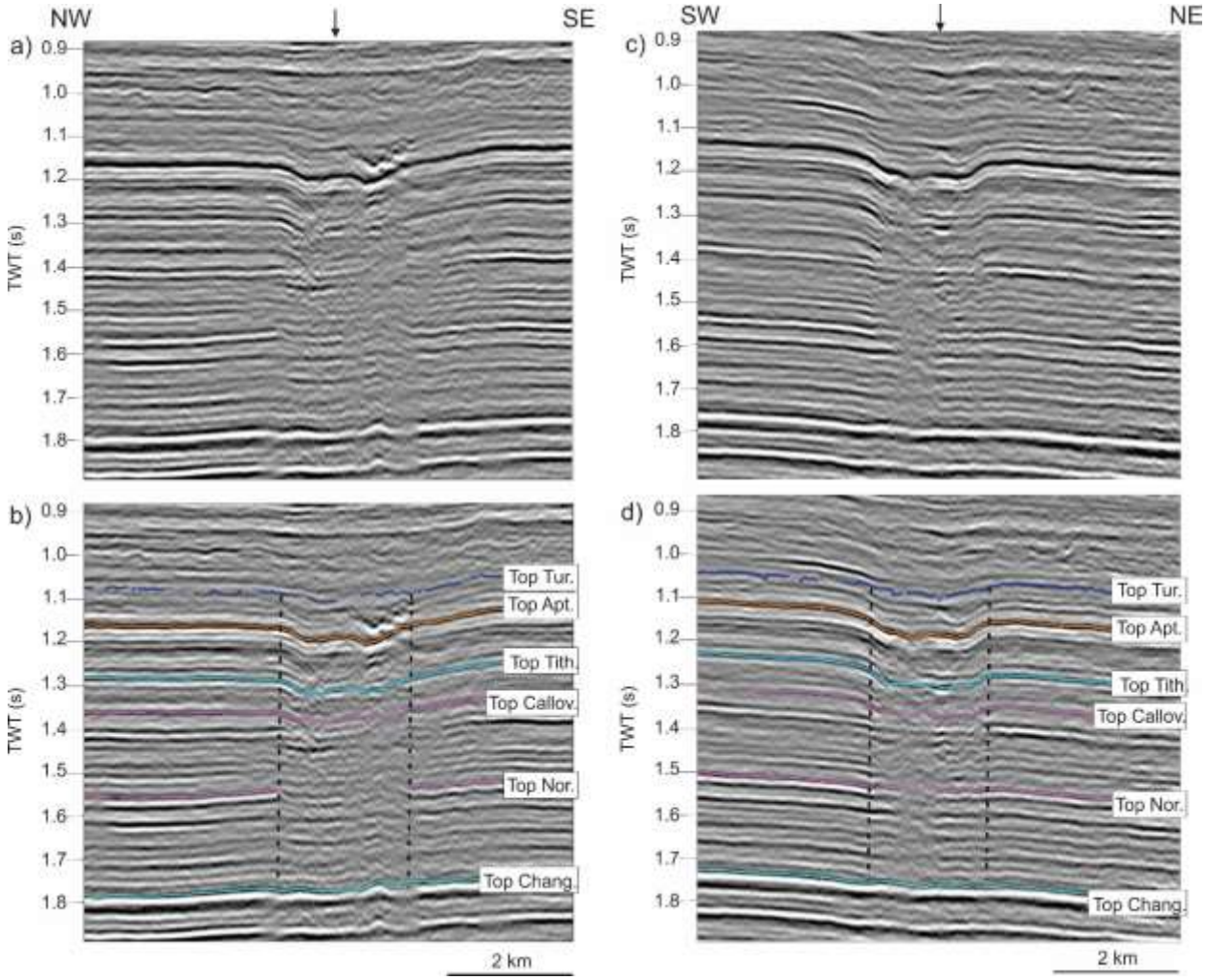

Figure 8

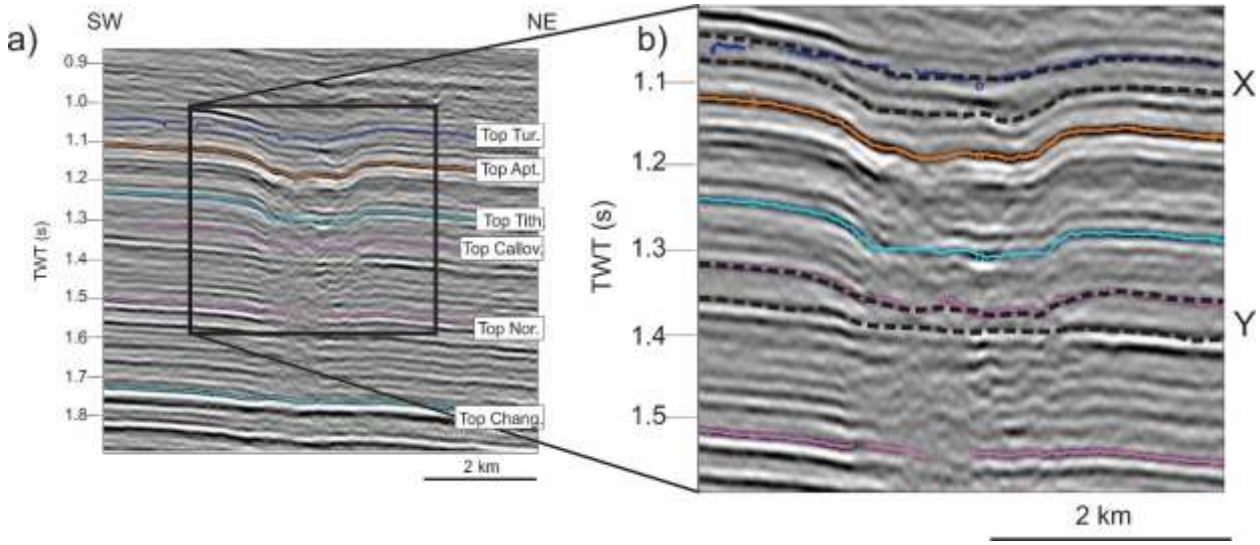

Figure 9

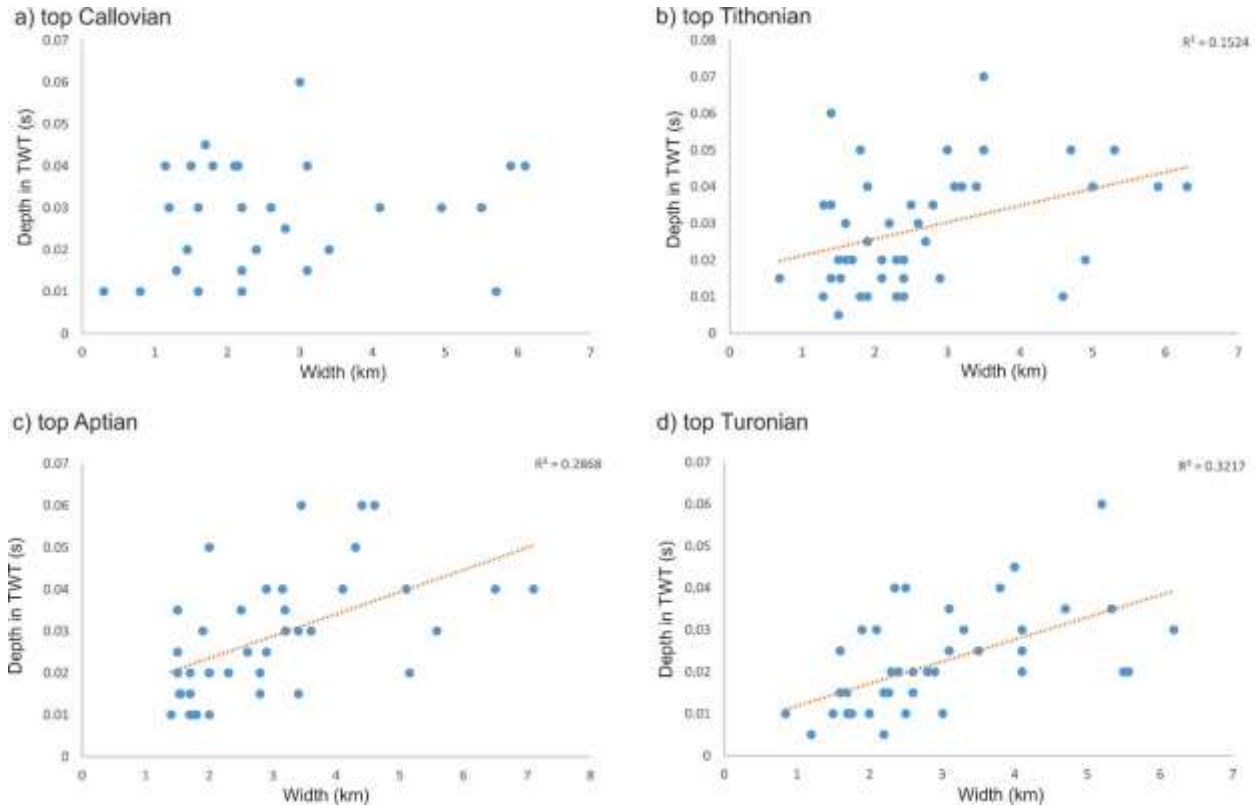
a) top Callovian
Depth in TWT (s)
Width (km)
b) top Tithonian
R² = 0.1524
Depth in TWT (s)
Width (km)
c) top Aptian
R² = 0.2868
Depth in TWT (s)
Width (km)
d) top Turonian
R² = 0.3217
Depth in TWT (s)
Width (km)

Figure 10

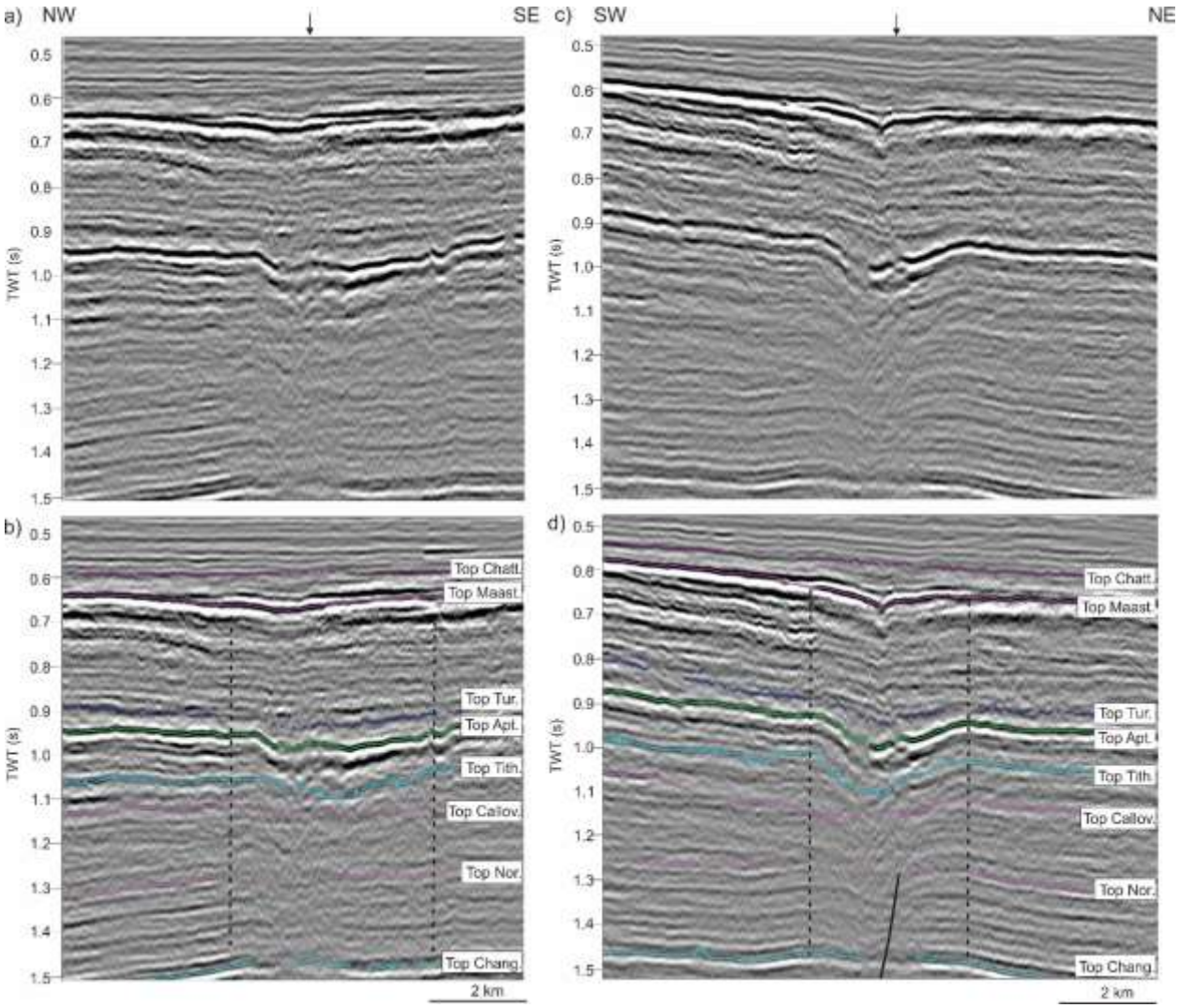
a) NW
SE
c) SW
NE
TWT (s)
b)
d)
Top Chatt.
Top Maast.
Top Tur.
Top Apt.
Top Tith.
Top Callov.
Top Nor.
Top Chang.
2 km

Figure 11

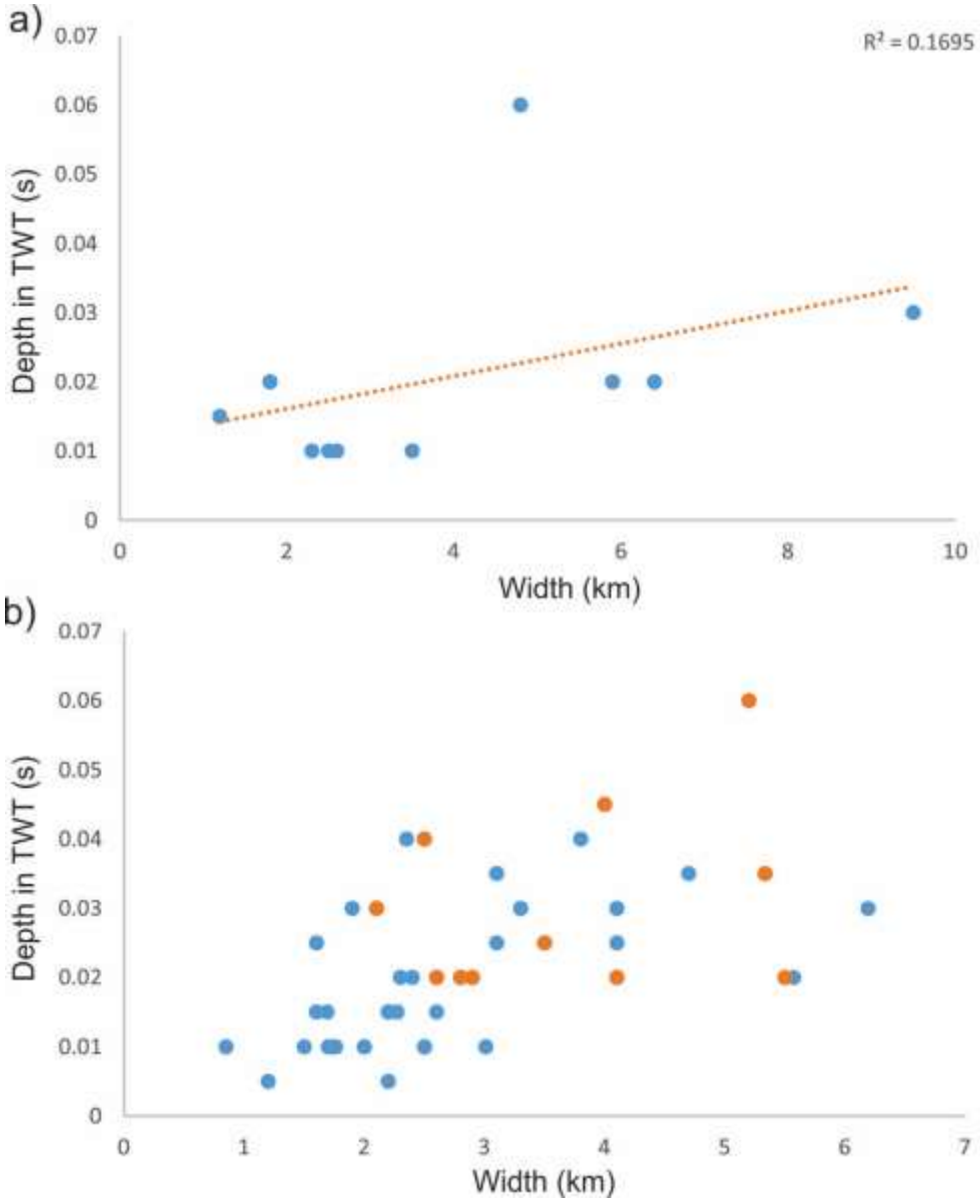
a)
R² = 0.1695
Depth in TWT (s)
0.07
0.06
0.05
0.04
0.03
0.02
0.01
0
0
2
4
6
8
10
Width (km)
b)
Depth in TWT (s)
0.07
0.06
0.05
0.04
0.03
0.02
0.01
0
0
1
2
3
4
5
6
7
Width (km)

Figure 12

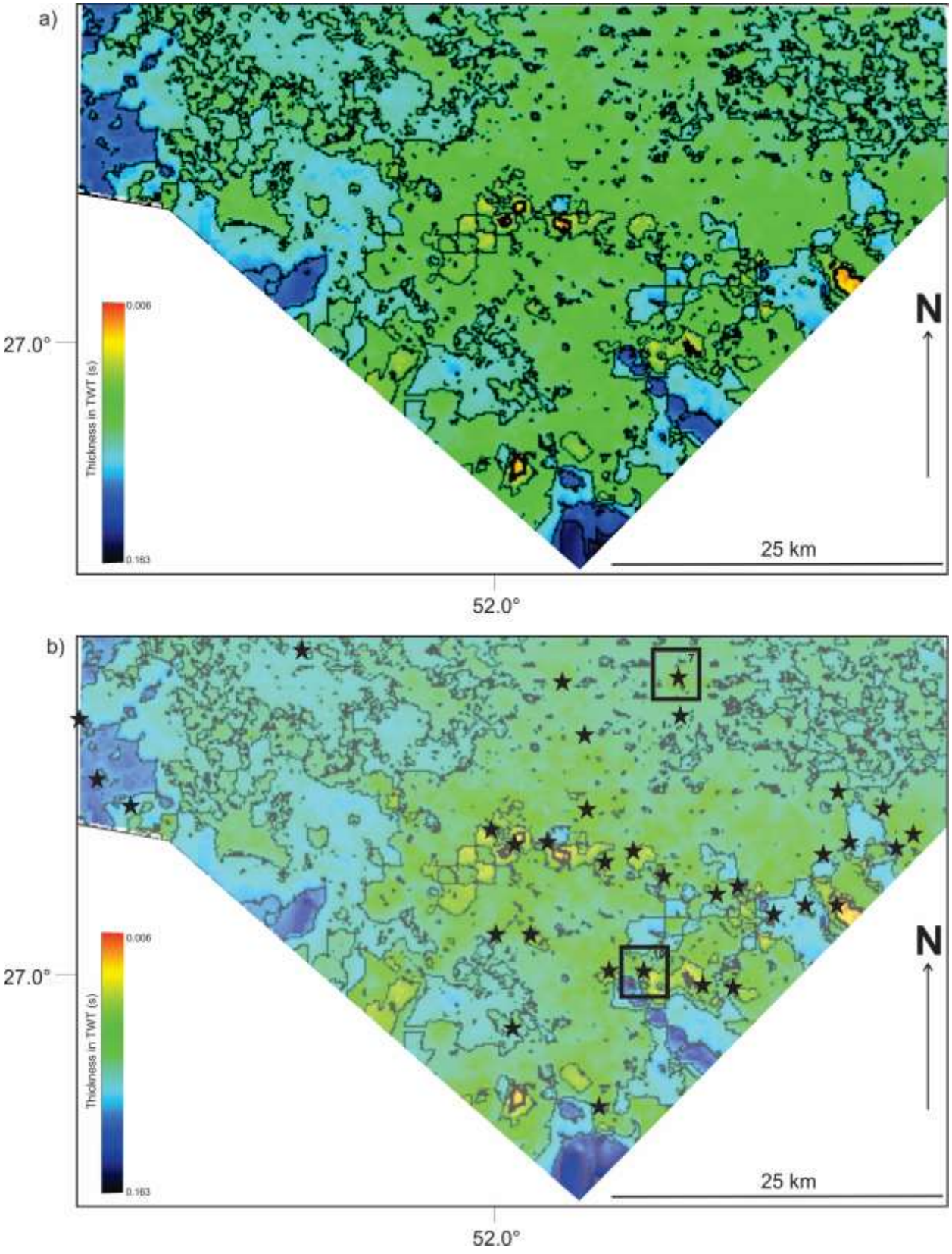
a)
27.0°
0.006
Thickness in TWT (s)
0.163
N
25 km
52.0°
b)
27.0°
0.006
Thickness in TWT (s)
0.163
N
25 km
52.0°

Figure 13

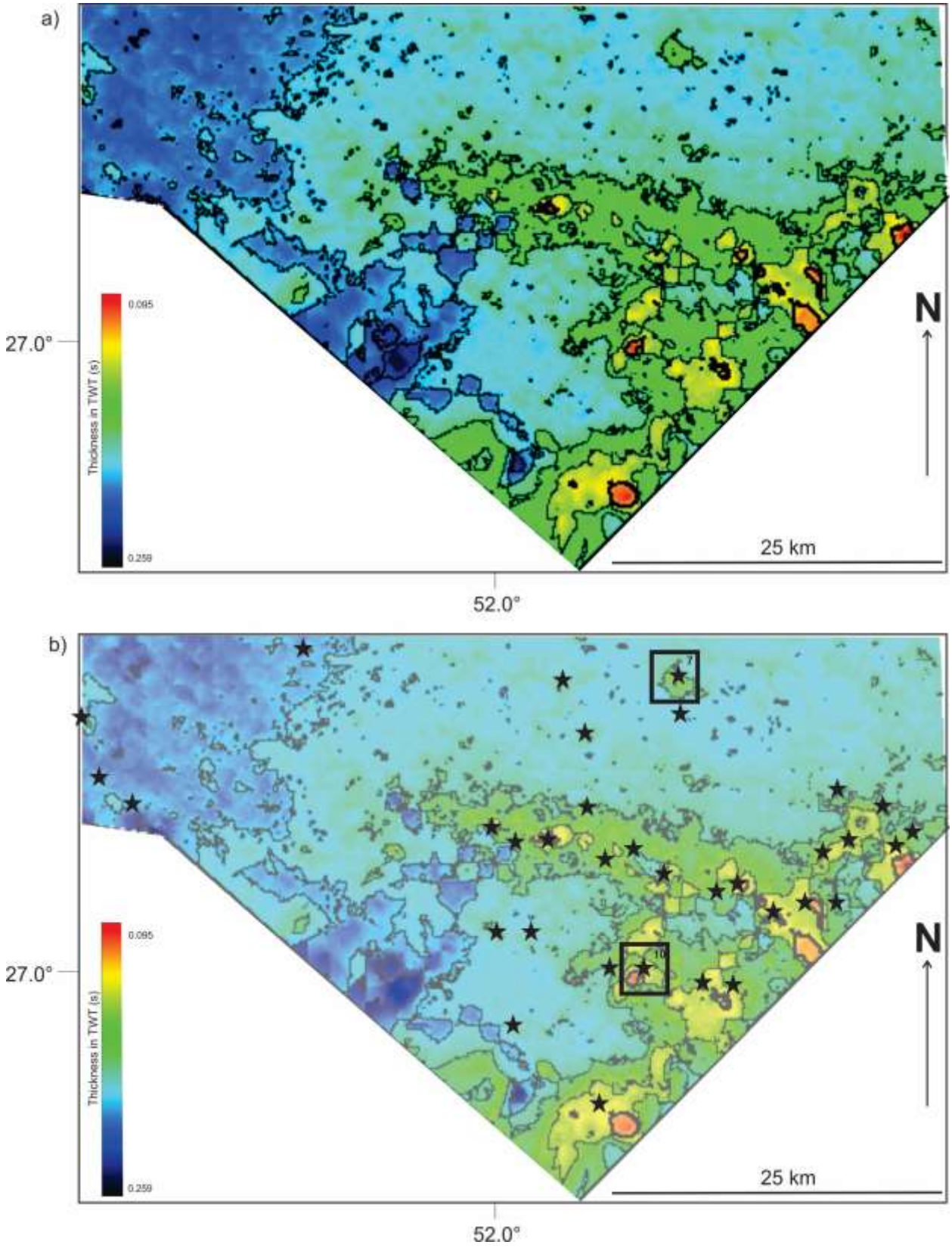
a)
27.0°
0.095
Thickness in TWT (s)
0.259
N
25 km
52.0°
b)
27.0°
0.095
Thickness in TWT (s)
0.259
N
25 km
52.0°

Figure 14

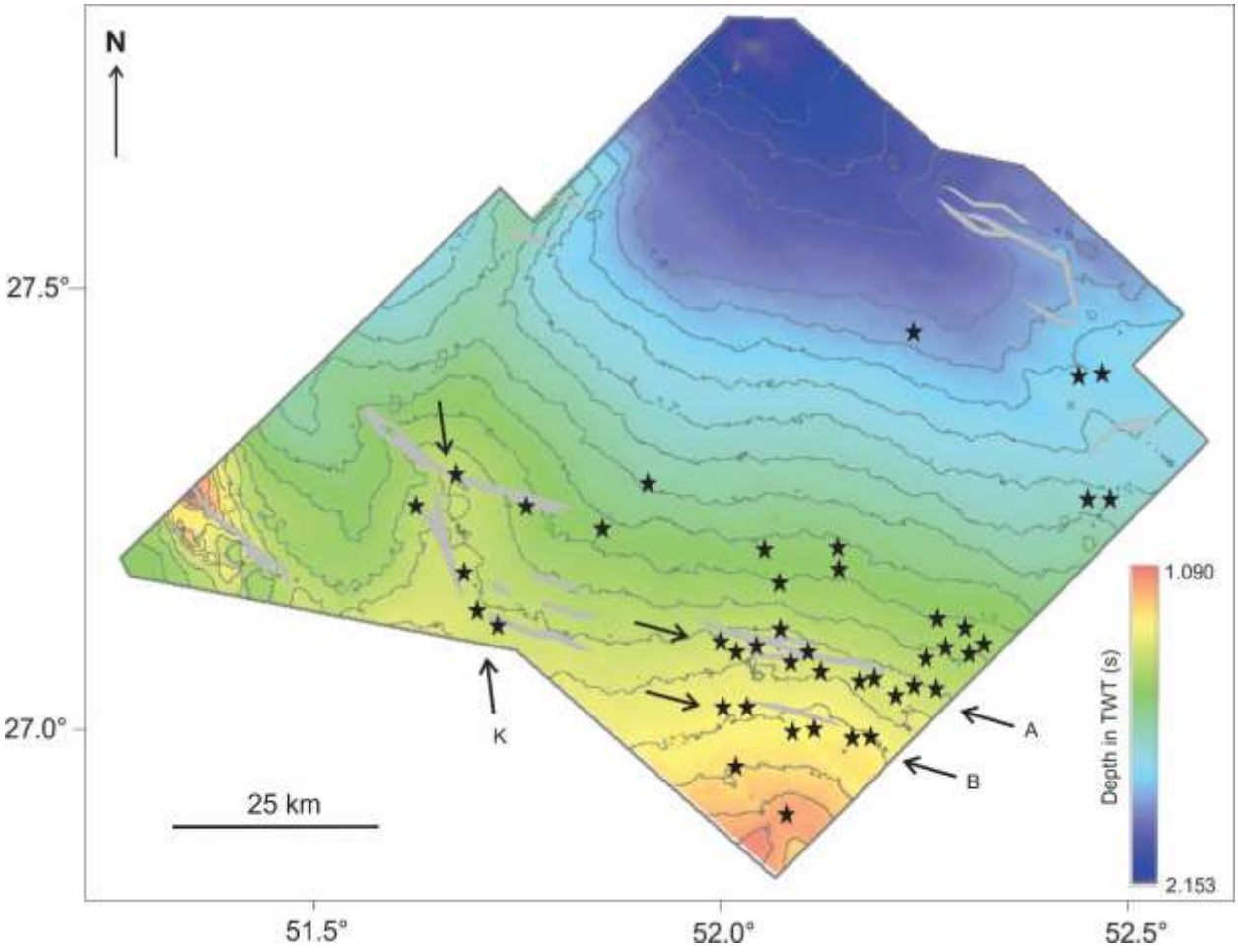

Figure 15

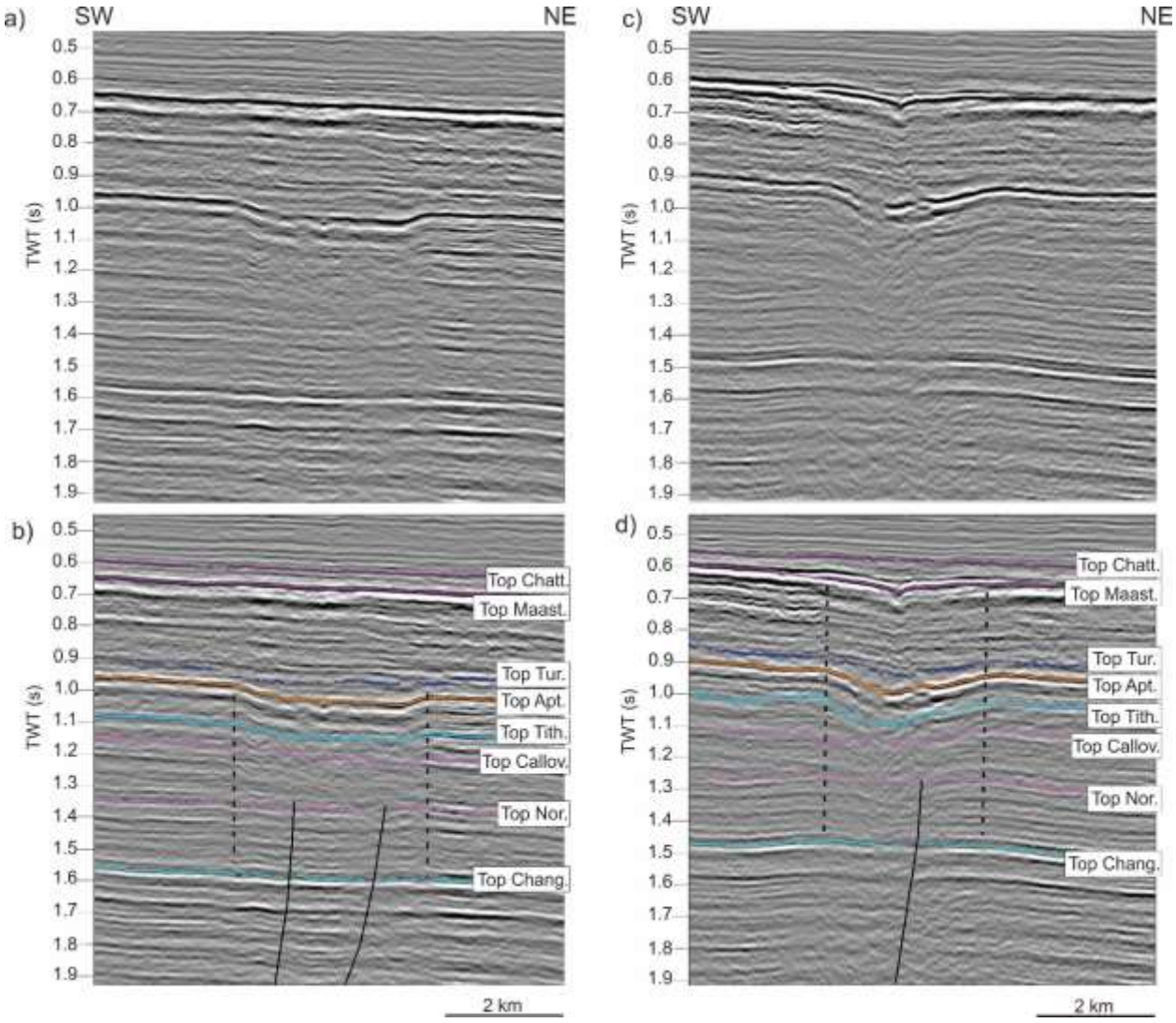
a)
SW
NE
TWT (s)
0.5
0.6
0.7
0.8
0.9
1.0
1.1
1.2
1.3
1.4
1.5
1.6
1.7
1.8
1.9
b)
Top Chatt.
Top Maast.
Top Tur.
Top Apt.
Top Tith.
Top Callov.
Top Nor.
Top Chang.
2 km
c)
SW
NE
d)
Top Chatt.
Top Maast.
Top Tur.
Top Apt.
Top Tith.
Top Callov.
Top Nor.
Top Chang.
2 km

Figure 16

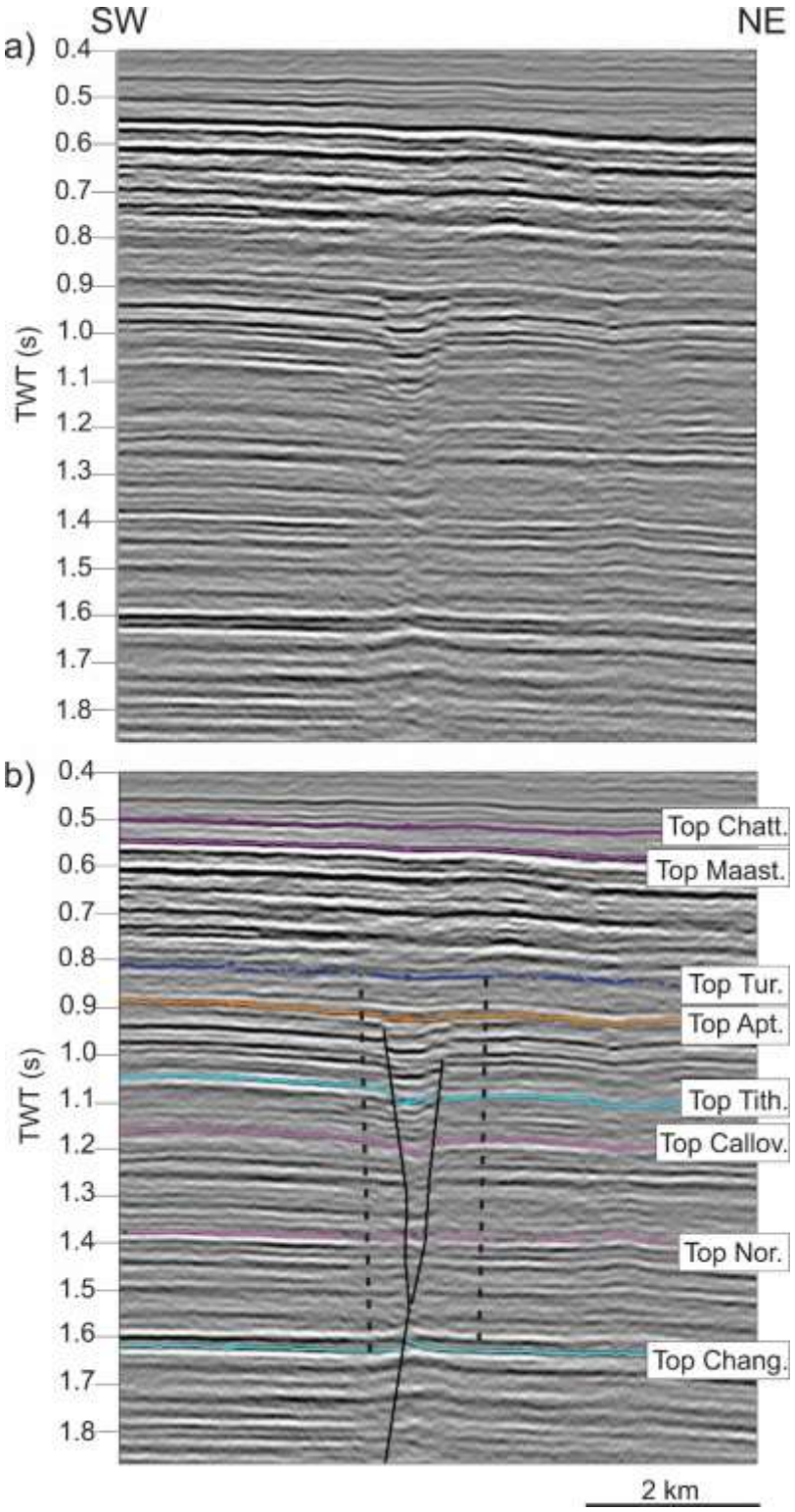
SW
NE
a)
b)
TWT (s)
0.4
0.5
0.6
0.7
0.8
0.9
1.0
1.1
1.2
1.3
1.4
1.5
1.6
1.7
1.8
Top Chatt.
Top Maast.
Top Tur.
Top Apt.
Top Tith.
Top Callov.
Top Nor.
Top Chang.
2 km

Figure 17

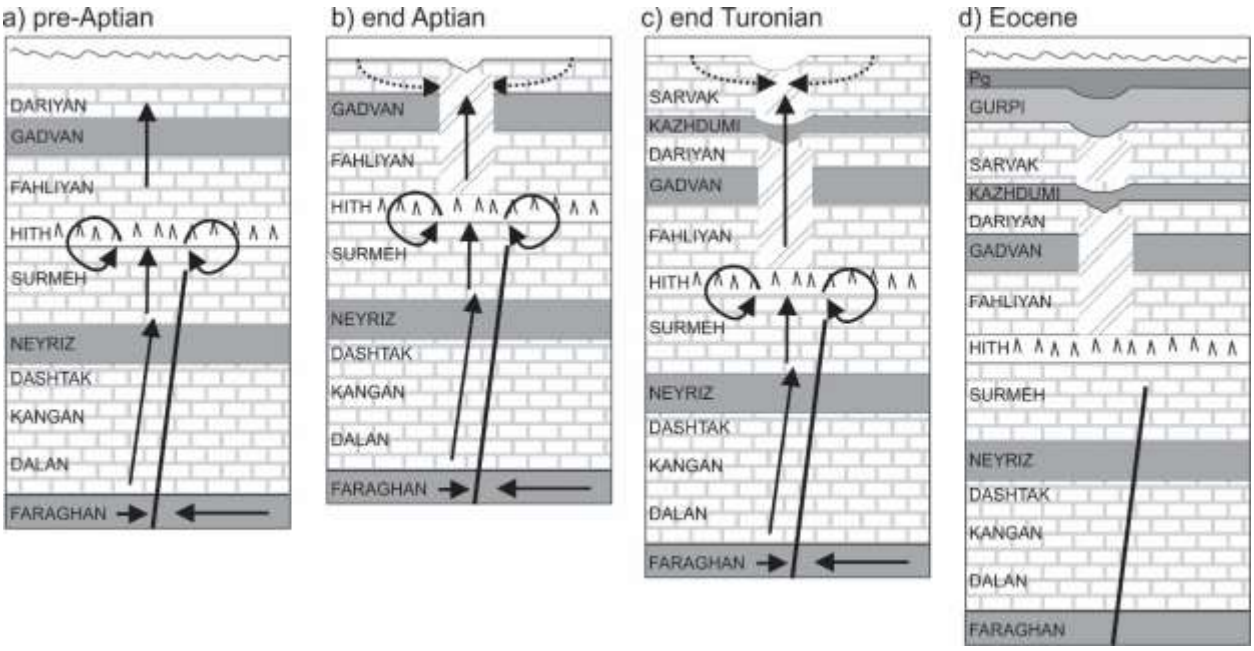
a) pre-Aptian
DARIYAN
GADVAN
FAHLIYAN
HITH
SURMEH
NEYRIZ
DASHTAK
KANGAN
DALAN
FARAGHAN
b) end Aptian
GADVAN
FAHLIYAN
HITH
SURMEH
NEYRIZ
DASHTAK
KANGAN
DALAN
FARAGHAN
c) end Turonian
SARVAK
KAZHDUMI
DARIYAN
GADVAN
FAHLIYAN
HITH
SURMEH
NEYRIZ
DASHTAK
KANGAN
DALAN
FARAGHAN
d) Eocene
Pg
GURPI
SARVAK
KAZHDUMI
DARIYAN
GADVAN
FAHLIYAN
HITH
SURMEH
NEYRIZ
DASHTAK
KANGAN
DALAN
FARAGHAN